Fluid dynamic characterization of single- and multiphase flow in structured porous media

Master Thesis

Author(s):
Häfeli, Richard

ETH
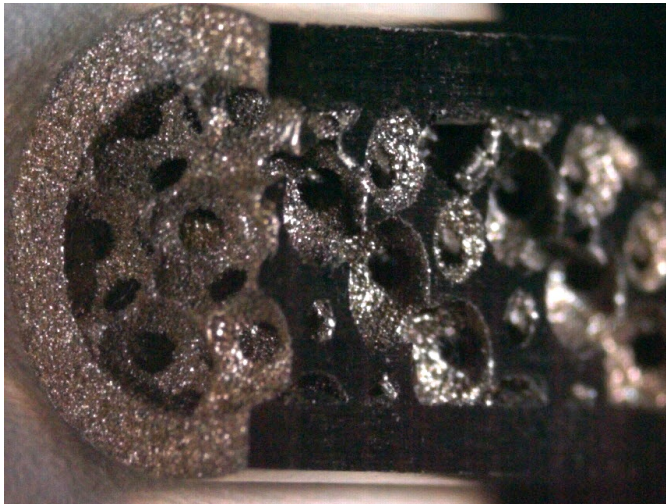Eidgenössische Technische Hochschule Zürich
Swiss Federal Institute of Technology Zurich

Institute of Process Engineering

Fluid Dynamic Characterization
of Single- and Multiphase Flow
in Structured Porous Media

Richard Häfeli
Supervisor: Dr. sc. ETH Cédric Hutter

Master Thesis, August 2010

Transport Processes and Reactions Laboratory

Abstract

Continuous tubular reactors have several advantages over batch reactors like increased safety, better heat transfer and more constant product quality. The LTR lab investigates tubular reactors with a highly porous foam-like packing produced by selective laser sintering (SLS). In this thesis, the fluid dynamic performance of different packings of 50mm length is investigated. Properties of primary interest are mixing behavior and residence time distribution (RTD).

In the first series of measurements, the radial mixing performance is measured by laser induced fluorescence (LIF) and a wire-mesh sensor (WMS). As the results are not identical to each other, LIF is preferred because it has a higher resolution and is broadly accepted as the standard method.

Regarding the mixing performance of the SLS foam it is shown that at high flowrates the coefficient of variation (CoV) is reduced to a value of 0.08. In literature [38] a CoV of 0.05 is already considered as homogeneous.

In the second part, the axial dispersion behavior is assessed using the wire-mesh sensor. Delgado [2] summarized that the measurement section for axial dispersion has to be long enough. We propose that when measuring axial dispersion, the hydrodynamic entrance length needs to be adressed. As a result of the axial dispersion measurements an empiric correlation between dispersion coefficient and Reynolds number is presented. It is concluded that for plug flow behavior a long reactor with high flowrate is in favorable over a short reactor with low flowrate.

Axial dispersion behavior changes when a second phase is added to the liquid flow. The wire-mesh sensor is used to measure axial dispersion of the liquid phase in a bubbly flow of air and water. As the WMS measures at 8×8 points, the noise of the signal is reduced compared to standard electrodes. Some scattering in the measured dispersion coefficients is still observed, making it difficult to draw conclusions about the exact behavior in two-phase flows.

Contents

List of Figures

List of Tables

Notation

Abbreviations

A/D	Analog to digital converter
CCD	Charge coupled device
fps	Frames per second
LIF	Laser induced fluorescence
LTR	Laboratory for transport processes and reactions
Nd:YAG	Neodymium-doped yttrium aluminium garnet ($Y_3Al_5O_{12}$) crystal
PIV	Particle image velocimetry
RhB	RhodamineB
RTD	Residence time distribution
sccm	Standard cubic centimeters per minute
SLS	Selective laser sintering
WMS	Wire-mesh sensor

Greek Letters

η	Dynamic viscosity	[kg/m·s]
ϵ	Porosity of solid packing	[-]
ν	Kinematic viscosity	[m^2/s]
ρ	Density	[kg/m^3]
$\sigma(c)$	Standard deviation of variable c	[kg/m^3]
τ	Mean residence time	[s]

Latin Letters

CoV	Coefficient of Variation	[-]
c	Concentration of tracer substance	[g/l]
d	Inner diameter of pipe / packing	[m]
d_{pore}	Pore diameter	[m]
D_L	Longitudinal (axial) dispersion coefficient	[m^2/s]
D_m	Molecular diffusion coefficient	[m^2/s]
$E(t)$	Residence time distribution / Pulse response	[1/s]
$F(t)$	Step-response	[-]
f	Fanning friction factor	[-]
i	Intensity of light recorded by LIF camera	[a.u.]
I	Current flowing through one node of WMS	[A]
$\hat{I}$	Digitalized signal of I	[A]
L	Length of packing	[m]
m	Characteristic slope of A/D converter	[-]
n	Number of measurement frames	[-]
ΔP	Pressure drop	[Pa]
Pe_{pore}	Pore Peclet number	[-]
Re	Empty pipe Reynolds number	[-]
Re_{pore}	Pore Reynolds number	[-]
Sc	Schmidt number	[-]
u	Interstitial velocity	[m/s]
v	Superficial velocity	[m/s]
V_R	Reactor volume	[m^3]
$\dot{V}$	Volume flow	[m^3/s]
x	Coordinate in axial direction	[m]
y	Coordinate in radial direction	[m]
z	Coordinate in radial direction	[m]
$<c>$	Spatial mean of c	[kg/m^3]
$\bar{c}$	Temporal mean of c	[kg/m^3]

Subscript and Superscript

high	Time averaged value in the calibration with high concentration
inlet	Variable measured at the inlet of the packing
outlet	Variable measured at the outlet of the packing
L	Longitudinal
low	Time averaged value in the calibration with low concentration
pulse	Pulse experiment
step	Step experiment

Chapter 1

Introduction

1.1 Background

There is a trend in the chemical industry to go from large scale batch to small continuous reactors. Continuous reactors are mainly established in the production of goods with high demand, like petroleum and fertilizer. For products of smaller throughput, there have been extensive research activities in the field of micro-reactors. Till this date it is however not possible to apply this reactor concept in industrial scale because of the low throughput. The research focus is therefore shifted towards the milli-scale. These reactors combine the advantages of micro systems with higher throughput and lower pressure drop. The system investigated in this thesis uses a tubular reactor of 7mm diameter which carries a structured packing. The very high area to volume ratio makes it applicable also for highly exothermic reactions. A higher selectivity of the reaction can be promoted by the isothermal conditions which are ensured by the high heat transfer coefficient. Further the thermal safety is increased in comparison to batch reactors because the milli-reactor has a smaller volume with more surface for heat exchange.

The structured packing in the tubular reactor improves mixing, heat transfer and plug flow behavior. Several industrial mixing devices are available for different applications. In our case a structured packing was produced imitating a metallic foam. Metallic foams are known from lightweight construction, as heat exchanger inserts and as catalyst support. A detailed summary about the manufacturing of metallic foams was published by Banhart[15]. One drawback of metallic foams is that one is limited in the manufacturing

process. By Selective Laser Sintering (SLS) we have the possibility to design packings of arbitrary shape. This allows us to investigate the effect of small changes in the packing geometry on the flow. A further advantage of SLS reactors is that they have a fixed connection to the wall, what was shown to have a major impact on the heat transfer coefficient[40].

1.2   Objectives

The objectives of this thesis are in a first step to characterize the radial mixing performance of a structured foam and compare it to industrially available static mixers. Two measurement methods should be applied for this measurement. The standard method is Laser Induced Fluorescence. We intend to also measure radial dispersion with a wire-mesh sensor, recently developed by Viereck [42], and compare the two measurement techniques.

In the second part of the thesis the axial dispersion within a milli-scale reactor with structured foam packing has to be investigated. These measurements should be carried out using two wire-mesh sensors at the inlet and the outlet of the packing. After measuring axial dispersion in a single-phase flow, the method should be applied to a two-phase flow of air and water. With common plate electrodes the measured conductivity is very much disturbed by the gas phase. With the wire-mesh sensor it is possible to simultaneously measure the conductivity at 8×8 point with a frequency of 10kHz. The idea of this approach is that the influence of the bubbles on the signal can be filtered out in a way that only the liquid phase is observed.

Chapter 2

Theory

This Chapter describes the required background for the understanding of transport phenomena in porous media. In a tubular reactor there is dispersion in axial and radial direction. The axial dispersion determines the residence time distribution, which affects the selectivity of a reaction. The radial dispersion is important concerning momentum exchange between the center and the boundary, which also leads to a narrower residence time distribution by forcing a flat velocity profile.

2.1   Radial Dispersion

Dispersion is the distribution of a set of fluid elements over a broader range by mass transfer. Initially segregated substance is radially mixed when flowing through a structured packing, like shown in Figure 2.1.
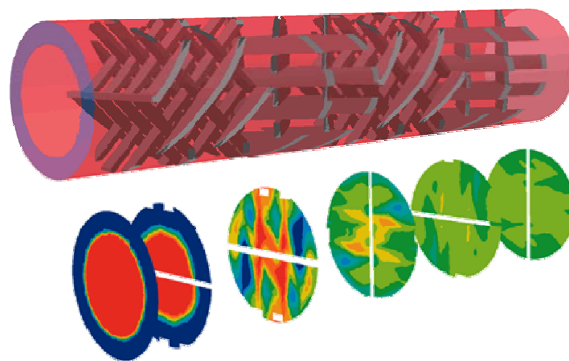
Figure 2.1: Illustration of radial dispersion within a structured packing.

3

The two types of mass transfer involved in radial mixing are diffusion and convection. The mass transfer by convection can again be subdivided into the effects of lamination and turbulence. This leads to three mechanisms of radial dispersion which can be identified:

- Diffusion

- Lamination

- Turbulence

Lamination is when fluid is separated by a solid structure and rearranged further downstream. For dispersion by lamination effects it is possible to design packings accordingly whereas turbulence leads to dispersion independent of the location. For the diffusion mechanism

In contrast to axial dispersion there are no satisfying models available describing radial dispersion. The usual way to describe radial dispersion is to inject a tracer in front of a packing and measure the distribution over the cross-section at the outlet. A prevalent technique for measuring concentration profiles is LIF. This measurement technique is also used in this thesis, in combination with a WMS. The measurement techniques are described in section 3.1. From collected pictures a criterion has to be found upon which one decides whether the achieved degree of homogenization is satisfactory or not. Hiby [27] published a good summary on definitions of mixing performance. One way is to use the *Coefficient of Variation* (CoV), which is given by the spatial standard deviation of the concentration normalized by the spatial mean concentration as in equation (2.1).

$$CoV = \frac{\sigma(\bar{c})}{<\bar{c}>} = \frac{\sqrt{\frac{1}{n} \cdot \sum_{i=1}^{n}(\bar{c} - <\bar{c}>)^2}}{<\bar{c}>} \qquad (2.1)$$

where σ is the standard deviation, $\bar{c}$ is the temporal mean of the concentration c, $<\bar{c}>$ is the spatial mean over the cross-section of the temporal mean and n the number of pixels.

Note that first the single frames are averaged in time and then the standard deviation of this mean picture is calculated. A low value of the CoV means that the tracer distribution is very homogeneous in the measured cross section.

2.2   Axial Dispersion

Running chemical reactions in tubular reactors it is of high importance to have a narrow residence time distribution, i.e. having small axial dispersion. In the case of axial dispersion three mechanisms of mass transfer were identified:

- Diffusion

- Non-uniform velocity profile over cross-section

- Turbulence

The effect of diffusion is shown in the results to play a minor role in the system that was investigated.

The mechanism of non-uniform velocity profile over the cross-section is always present because of the no-slip condition of the flow at the boundaries. In an empty pipe with laminar flow the velocity profile is known to be parabolic, leading to a dispersion in axial direction. With higher Reynolds numbers the velocity profile is flattened leading to less axial dispersion. Using structured packings can further help to increase momentum exchange from the center of the tube to the boundary, leading to less axial dispersion. The third mechanism of axial dispersion is the turbulent mixing. The stochastic nature of convection by turbulent flow makes its influence comparable to molecular diffusion. In this thesis the velocity profile over the cross-section is assumed to be uniform, which allows to use the dispersion model.

The subchapters that follow introduce the theory that is required to model axial dispersion. Further the procedure used for deconvolution of measurement signals is shown.

2.2.1   Residence Time Distribution

An important concept in continuous reactors is the residence time distribution. When running a chemical reaction in a continuous reactor, i.e. a continuously stirred tank reactor, one is interested in how long the substance remains in the reactor. In an ideal case without dead zones the mean

residence time in the reactor is given by:

$$\tau = \frac{V_R}{\dot{V}} \tag{2.2}$$

When a reactor has dead zones which are not streamed, a mean residence time smaller than the one given by eq. (2.2) is measured.

In practice it can be observed that not all fluid elements stay in the reactor for the same time. Some might go directly from the inlet to the outlet while others stay in the reactor for a long time. This leads to the RTD, usually assessed by injecting a pulse of tracer at time $t = 0$. Measuring the concentration of tracer at the outlet as a function of time $c_{outlet}^{pulse}(t)$, the RTD can be calculated:

$$E(t) = \frac{c_{outlet}^{pulse}(t)}{\int_0^\infty c_{outlet}^{pulse}(t) \cdot dt} \tag{2.3}$$

Injecting a step change at the inlet one measures at the outlet the $F(t)$ curve:

$$F(t) = \frac{c_{outlet}^{step}(t)}{\int_0^\infty c_{outlet}^{step}(t) \cdot dt} \tag{2.4}$$

The $F(t)$ curve can also be calculated from a pulse experiment by integrating eq. (2.3).

$$F(t) = \int_0^t E(t) \cdot dt \tag{2.5}$$

Generally the RTD function $E(t)$ can be of arbitrary shape. In practice one often tries to describe the RTD by a function with few parameters. Models often used are the Gaussian distribution, log-normal distribution, the tanks-in-series model, or the dispersion model. In this thesis the dispersion model is used.

2.2.2 Dispersion Model

The system under investigation is a tubular reactor of length L. When assuming homogeneous flow and concentration over the cross-section this system can be modeled one-dimensional with u as the interstitial velocity. The nomenclature is shown in Figure 2.2.

In the dispersion model it is assumed that the axial mass transfer stemming
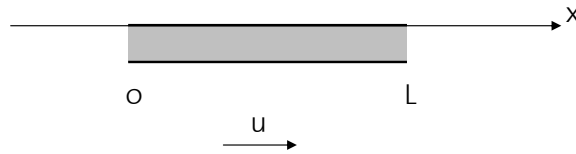
Figure 2.2: 1D model of tubular reactor.

from turbulence can be modeled similar to diffusion. The governing equation for the concentration of a species under the influence of dispersion and convection with velocity u is:

$$\frac{\partial c}{\partial t} = D_L \cdot \frac{\partial^2 c}{\partial x^2} - u\frac{\partial c}{\partial x} \tag{2.6}$$

where $c(x,t)$ is the concentration of a tracer and D_L is the dispersion coefficient, accounting for mass transfer by both diffusion and turbulence. To solve this differential equation we assume that the velocity of the fluid is zero. Later the velocity is accounted for by changing the coordinates. Like this we can write the differential equation for the concentration as:

$$\frac{\partial c}{\partial t} = D_L \cdot \frac{\partial^2 c}{\partial x^2} \tag{2.7}$$

The solution to this equation depends on initial and boundary conditions. Boundary conditions can either be open or closed. Open boundary condition is to assume that the reactor is infinitely long. Closed boundary conditions correspond to a modeled length of $0 < x < L$, with plug-flow boundary conditions at the inlet and outlet, i.e. no backmixing. An analytical solution exists only for open-open[1] boundary conditions. The open-open boundary conditions are motivated physically by the assumption that one can have dispersion over the entrance and the exit of the reactor. The initial condition respected here is a pulse injected at the inlet at time $t = 0$. Mathematically this is represented by:

$$c(x,0) = f(x) = \delta(x) \text{ for } t = 0. \tag{2.8}$$

where $\delta(x)$ is the Dirac delta function. The solution of the differential equation (2.7) with general boundary conditions $f(x)$ is known from Evans [39]

---

[1]Open-open means open both on the left and on the right.

to be the following convolution integral:

$$c(x,t) = \int_{-\infty}^{+\infty} \frac{1}{\sqrt{4\pi D_L t}} \cdot exp\left(\frac{-(x-x')^2}{4D_L t}\right) \cdot f(x')dx' \qquad (2.9)$$

With the Dirac pulse of eq. (2.8) as boundary condition the solution for the concentration as a function of x and t is given by:

$$c(x,t) = \int_{-\infty}^{+\infty} \frac{1}{\sqrt{4\pi D_L t}} \cdot exp\left(\frac{-(x-x')^2}{4D_L t}\right) \cdot \delta(x')dx' \qquad (2.10)$$

$$= \frac{1}{\sqrt{4\pi D_L t}} \cdot exp\left(\frac{-x^2}{4D_L t}\right) \qquad (2.11)$$

A plot of the solution at times $t = 0, 1, ..., 5$s is shown in (Figure 2.3).
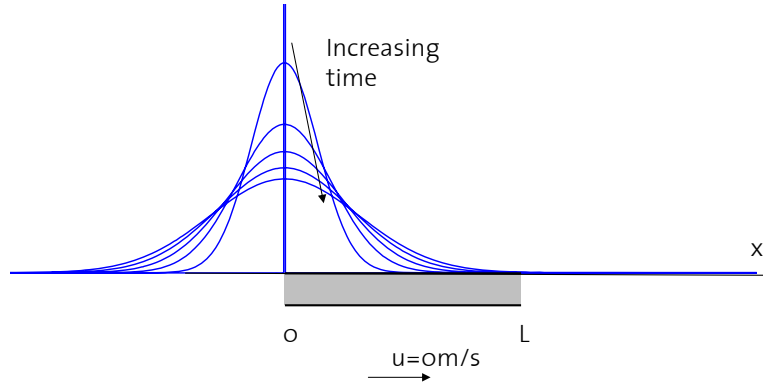
Figure 2.3: Axial concentration distribution $c(x)$ at times $t = 0, 1, ..., 5$s when fluid velocity is zero. Dispersion coefficient $D_L = 0.001\mathrm{m}^2/\mathrm{s}$.

This is still the solution for a velocity $u = 0$. In a normal tubular reactor however the velocity is non-zero. In that case the solution for the concentration is obtained by replacing x by $x - ut$.

$$c(x-ut,t) = \frac{1}{\sqrt{4\pi D_L t}} \cdot exp\left(\frac{-(x-ut)^2}{4D_L t}\right) \qquad (2.12)$$

Plotting this solution for times $t = 0, 1, ..., 5s$, we see a concentration profile moving in the positive x-direction as shown in Figure 2.4.

For the calculation of the RTD we are only interested in the concentration
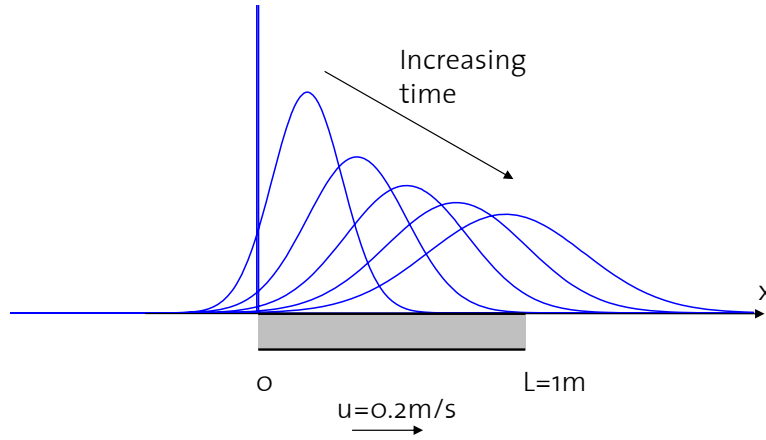
Figure 2.4: Axial concentration distribution $c(x)$ at times $t = 0, 1, ..., 5\text{s}$ when convection is included with $u = 0.2\text{m/s}$. Dispersion coefficient $D_L = 0.001\text{m}^2/\text{s}$.

at the reactor outlet, i.e. at $x = L$:

$$c(L - ut, t) = \frac{1}{\sqrt{4\pi D_L t}} \cdot exp\left(\frac{-(L - ut)^2}{4D_L t}\right) \qquad (2.13)$$

To calculate the RTD eq. (2.13) has to be entered in eq. (2.3). The numerical solution of the integral in the denominator is given by:

$$\int_0^{+\infty} c(L - ut, t) = \frac{1}{u} \qquad (2.14)$$

With this result the RTD can be written as:

$$E(t) = \frac{c(L - ut, t)}{1/u} = \frac{u}{\sqrt{4\pi D_L t}} \cdot exp\left(\frac{-(L - ut)^2}{4D_L t}\right) \qquad (2.15)$$

This result is also shown in Levenspiel [34] but without derivation.

Defining $\tau = L/u$, eq. (2.15) can be rewritten as:

$$E(t) = \frac{1}{\tau \cdot \sqrt{4 \cdot \pi \cdot \frac{D_L}{u \cdot L} \cdot t/\tau}} \cdot exp\left(\frac{-(1 - t/\tau)^2}{4\frac{D_L}{u \cdot L} \cdot t/\tau}\right) \qquad (2.16)$$

Now the dispersion behavior is described by only two parameters: mean residence time τ and the dimensionless group D_L/uL which is sometimes

called vessel dispersion number[2]. The vessel dispersion number determines the width of the residence time distribution. Figure 2.5 shows residence time distribution curves when the dispersion coefficient is varied.
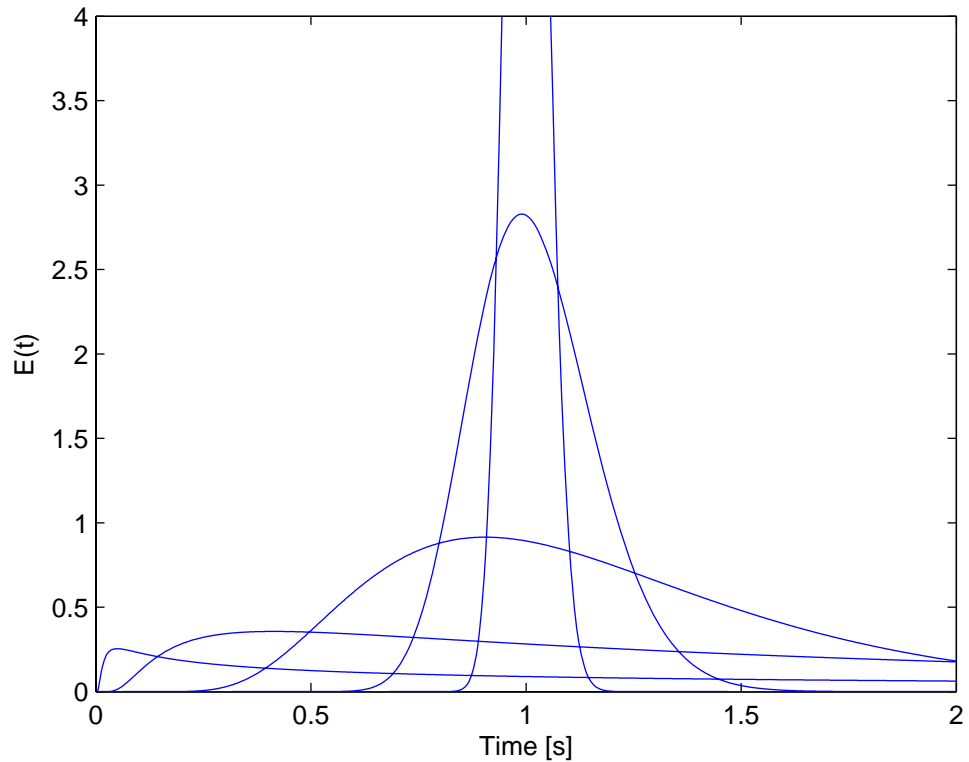
Figure 2.5: Residence time distribution according to the dispersion model. Parameters used are velocity $u = 1\text{m/s}$ and $L = 1\text{m}$. The vessel dispersion number is varied from $D_L/uL = 0.001$ for the narrow distribution and $D_L/uL = 10$ for the broad distribution.

Levenspiel [34] mentions that the RTD modeled with the dispersion model with open-open boundary conditions is not exactly the RTD. The reason is that at the inlet of the reactor we have a Dirac pulse $c(x, t = 0) = \delta(x)$ and not $c(x = 0, t) = \delta(t)$. Figure 2.4 shows that at the reactor inlet the tracer disperses back and the signal at the inlet is non-zero for positive times. This effect is more pronounced with higher dispersion coefficient. This is a general drawback of the dispersion model and it is important to keep this in mind. For small extents of dispersion however this effect can be neglected.

---

[2]Sometimes the inverse of the vessel dispersion number is taken and called Peclet number or Bodenstein number. In this thesis we call D_L/uL the vessel dispersion number

For large extends of dispersion the closed-closed boundary conditions can be used. There the boundary conditions prohibit mass transfer over the inlet and the concentration simulated at the outlet corresponds to the RTD. However for closed-closed boundary conditions no analytical solution exists. In our study the dispersion coefficients are considered to be small enough for the dispersion model to be used.

2.2.3   Evaluation of Pulse Experiments

For the measurement of axial dispersion usually pulse or step experiments are made. In principle also an arbitrary stochastic signal at the input can be used. The theory predicts that the concentration profile over time at the outlet is given by the convolution of the concentration profile at the inlet with the RTD function $E(t)$:

$$c_{outlet}(t) = \int_0^t c_{inlet}(t^*) \cdot E(t - t^*)dt^* \qquad (2.17)$$

The easiest case is when it is achieved to inject a Dirac-pulse at the inlet. In this case the residence time distribution $E(t)$ is given by the concentration profile at the outlet. When the inlet concentration profile is of arbitrary shape the two signals have to be deconvoluted. Two methods to do the deconvolution are investigated during this thesis. The first method is to transform equation (2.17) to frequency domain, where the convolution becomes a simple multiplication. The second method is to numerically determine $E(t)$ in a way that equation (2.17) is fulfilled. Using the dispersion model, which is described by only two parameters τ and D_L, it is possible to calculate $E(t)$ numerically. This method was already used by others, e.g. Nalitham [13].

An algorithm is implemented which varies the two parameters τ and D_L. A subfunction then calculates the residence time distribution $E(t)$ at these two parameters. The convolution of $E(t)$ with the inlet concentration gives a simulated outlet concentration. This simulated outlet concentration is than compared to the measured outlet concentration. Then the iteration on τ and D_L starts again until the two curves fit best in terms of root mean square difference. Figure 2.6 shows an example of a fit to a measured curve.

It turns out that this method is very robust and is also able to evaluate noisy data. In contrast to the method using Fourier transformation this
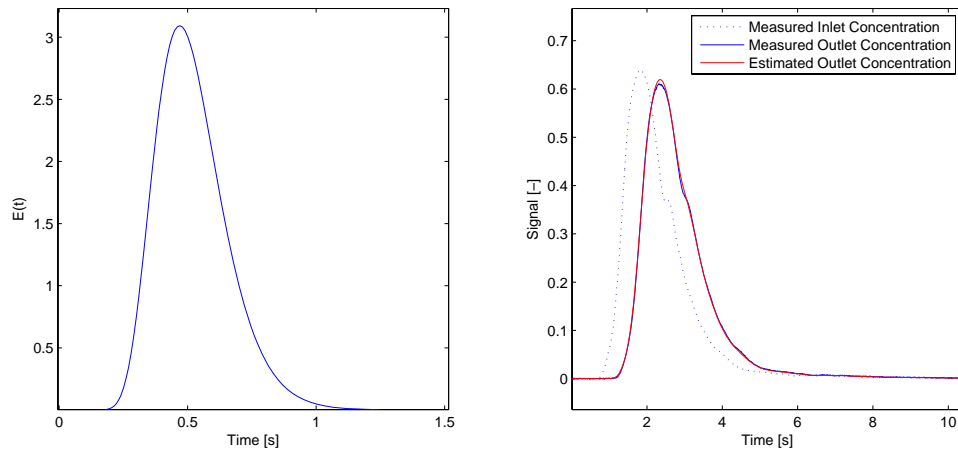
Figure 2.6: Left: Estimated residence time distribution $E(t)$. Right: Measured concentration profiles at inlet/outlet and convolution of estimated $E(t)$ with inlet concentration profile

method does not have any filters that require adjustment of parameters.

2.2.4   Dispersion in Two-Phase Flow

For real applications gas-liquid two phase flows are often encountered. One example is a reaction in the liquid phase with one gaseous educt. In that case the RTD of the liquid phase is of interest. Also the gas-phase has a certain RTD, which is however not of interest because it contains only one species.

Another objective of this thesis is therefore to investigate how the dispersion in the liquid changes with changing gas flowrate. In a microfluidic device Trachsel [14] observed a narrower RTD in two-phase flow than in the single phase flow. The flow in that micro device was in the Taylor flow regime. In this thesis the dispersion behavior is investigated in the bubbly flow regime. It This could lead to interesting applications where one uses a second phase only for tuning the RTD.

Chapter 3

Experimental

The two main measurement techniques used in this thesis for tomographic investigations are LIF and a WMS. The first subsection describes the measurement methods. In the second subsection the detailed experimental procedures and the post-processing is described. The overall plant is described in the third subsection. The end of this chapter then depicts the different investigated packings.

3.1 Measurement Techniques

3.1.1 LIF - Laser Induced Fluorescence

The first measurement technique used for tomographic investigations is LIF. A Nd:YAG laser produces a sheet of light with a wavelength of 532nm. A fluorescent dye flowing through the laser sheet is excited by the laser and emits light of a higher wavelength. The emitted light can then be recorded by a camera. Figure 3.1 shows the setup used in this thesis.

 When measuring in a round cross section one usually uses a view-cell that partly compensates the refraction of light.
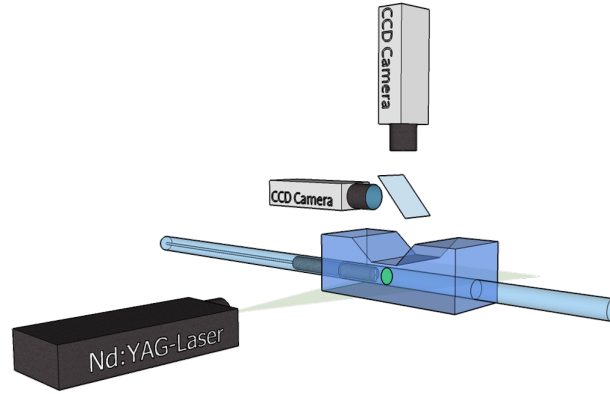
Figure 3.1: Setup for LIF measurements showing laser, laser sheet, packing, mirror and cameras (LIF and PIV)

3.1.2   WMS - Wire Mesh Sensor

For more than ten years wire-mesh sensors are used for tomographic investigations, mainly in two phase flows. A WMS for a pipe cross section of 7mm was developed in a previous work of the LTR lab by Viereck [42]. The principle of the WMS is based on the work by Prasser [11].

A wire-mesh sensor consists of two planes of wires forming a multi-dimensional electrode. The angle between the wires of the two planes is 90°. By measuring the current flowing from a wire of one plane to a wire of the second plane the conductivity is measured. For this, all other wires are grounded, which makes sure that the current is only flowing in the vicinity of the crossing point of the two wires, as shown in Figure 3.2. According to Viereck, the spacing between two parallel wires is 0.778mm and the axial spacing of the two wire planes is 0.6mm. The wires have a diameter of 50μm.

The electronic device allows to measure with a frequency of 10kHz. This means that at a flow velocity of 1m/s we have a resolution in axial direction of 0.1mm. This is better than the spatial resolution in radial direction. This implies that very accurate transient data can be measured. The electronic scheme is shown in Figure 3.3.
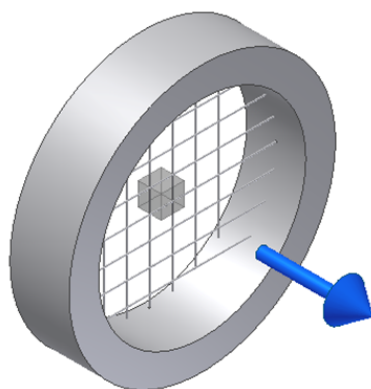
Figure 3.2: Wire Mesh Sensor
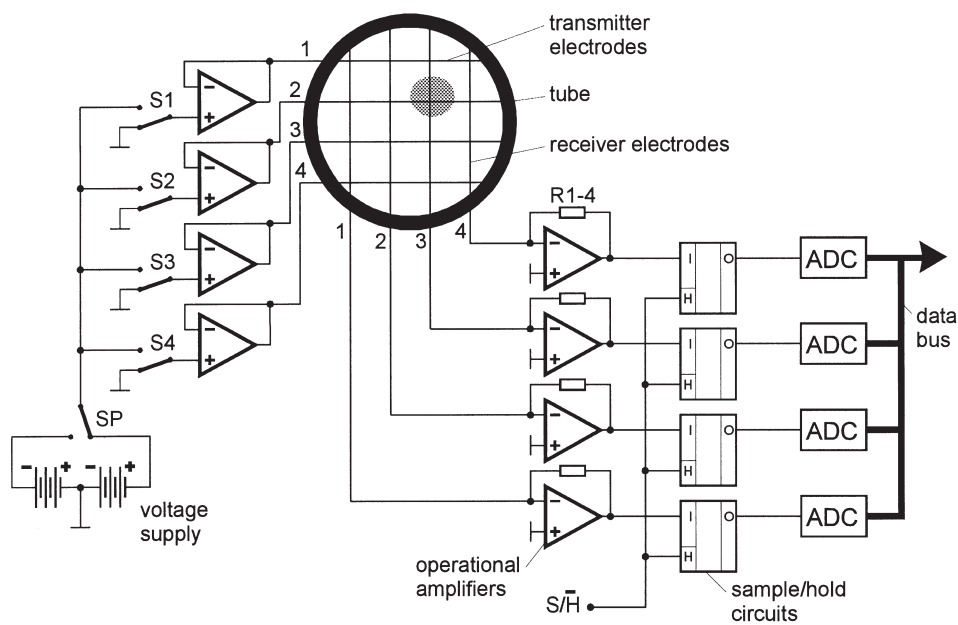
Figure 3.3: Simplified scheme of the electrode-mesh device.

3.2 Experimental Procedures

3.2.1 Radial Dispersion by LIF

In this thesis LIF is used to measure radial dispersion in static mixers of 50mm length. RhodamineB (RhB) is used as tracer substance. The Schmidt number in water is $Sc = \nu/D_m = 2300$. The tracer solution is injected by a capillary just in front of the packing. Flowing through the static mixer the tracer is dispersed over the cross-section. The concentration distribution is then observed in the laser sheet which is placed $0.5d$ downstream the exit of the packing. Ideally the laser sheet would be placed as near to the packing as possible. Other authors, like Wadley[24], measured $1d$ downstream. Like this the experiments do not only reflect the mixing by the packing but also some 'mixing-for-free' which occurs in the empty pipe. In the investigated packings of 50mm length the effect of the downstream mixing in the $0.5d = 3.5$mm empty pipe is considered to be negligible.
The CCD chip of a digital camera records the emitted light of the tracer which is reflected by a dichroic mirror. The setup shown in Figure 3.1 with two cameras and the dichroic mirror would in principle allow to do LIF and PIV[1] simultaneously. The frame rate of this setup is 4fps.

Two effects have to be considered in LIF experiments: spatial variation and temporal variation of the signal. A spatial variation of the light intensity i is also observed in a homogeneous solution. One of the reasons for this behaviour is that the laser sheet does not have the same intensity over the whole cross-section. Another reason is that the sensitivity of the camera is not equal for all pixels. This was incorporated by making two calibration measurements, one without tracer and one with a given tracer concentration C_{high}. For every pixel the intensity of light was then linearly interpolated with the two calibration measurements as shown in eq. (3.1).

$$c(t) = \frac{i(t) - i_{low}}{i_{high} - i_{low}} \cdot c_{high} \tag{3.1}$$

The temporal variation of the signal comes from pulse to pulse variation of the laser intensity which is roughly 1%. Because of this also a variation in brightness from frame to frame is observed. This is however not a problem, because only the information about the spatial segregation is of interest.

---

[1]PIV: Particle image velocimetry. Method used to measure velocity field.

A second post processing step is required because the laser sheet is observed from an angle of $0°$ and not from $60°$ relative to the axis of the reactor. The resolution is therefore not equal in both dimension. The 7mm cross section of the pipe contained 120×250 pixels what corresponds to a resolution of 0.03mm×0.06mm. This is coped with by adding a rectangular pattern into the measurement section as shown in Figure 3.4. The way
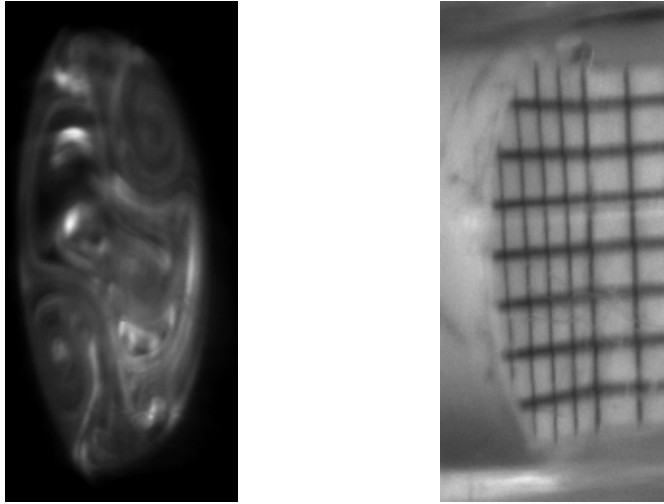
Figure 3.4: Left: LIF image showing the distribution of RhB tracer in the measurement cross-section. Right: rectangular pattern for mapping back the stretched image to a round image.

this pattern is stretched by viewing from the given angle it is possible to map back the LIF images to a round cross-section. The mapped coordinate system is shown in Figure 3.5.

However it has to be mentioned that mapping back is only used to select the points that are within the measurement section. Still in one direction the resolution is two times higher than in the other. This can lead to wrong estimates of the CoV. An improvement of the evaluation procedure would be to account for this fact by mapping the LIF images to a round cross-section with same number of pixels in both directions.

For every measurement series as much as 100 pictures were taken. After the post-processing described above, the temporal mean value is calculated for every pixel. From this mean picture the CoV is then calculated according to eq. (2.1).

The tracer flowrate is in all cases set by a syringe pump. For injection
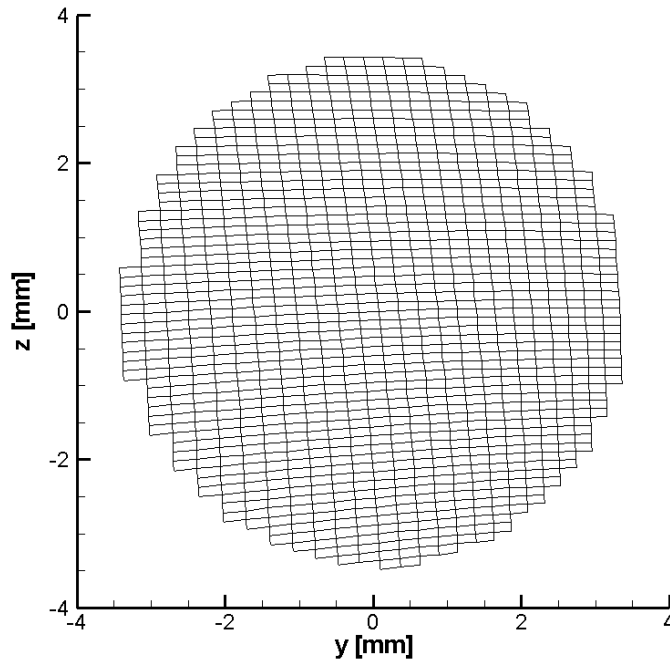
Figure 3.5: Coordinate system after mapping back of images.

of the tracer into the main stream two different capillaries are used. In previous measurements of the LTR lab a side injection capillary was used. This capillary was originally designed to allow fixation of an unstructured foam. For measurements with structured packings this is not necessary because our packing has a fixed connection to the wall. However for keeping our experiments comparable with the ones done for unstructured foams, two measurement campaigns are made. The reason to use the straight injection capillary is that it leads to a flowrate independent boundary condition at the inlet. Zalc [29] observed that the mixing performance can be a strong function of the injection location. Also for flow simulation the straight injection capillary is much easier to implement. The following two paragraphs summarize the measurement conditions with the respective capillary in detail.

Side Injection Capillary
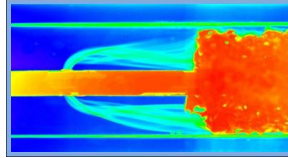
Figure 3.6: Side injection capillary used in LIF experiments.

The investigated main flowrate reached from 100ml/min to 2500ml/min. The tracer flowrate through the capillary is kept constant at 6ml/min. For the allowed concentration of tracer there is an upper limit to prevent over-exposure of the pictures. The concentration of RhB tracer at the highest flowrate is therefore set to 320mg/l. In order to keep the brightness of all pictures constant the concentration in the mixed condition is kept constant. This is achieved by adjusting the concentration of the tracer in the syringe.

Straight Injection Capillary
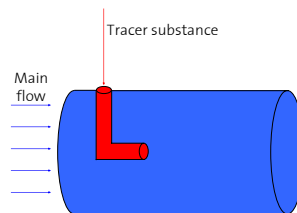
Figure 3.7: Straight injection capillary used in LIF and WMS experiments.

The investigated flowrate in the experiments with the straight injection capillary reach from 100ml/min to 2500ml/min. In order to have isokinetic conditions, the flowrate ratio was chosen as 1 : 100, i.e. the injection flowrate was 1ml/min to 25ml/min. This choice of flowrate ratio ensures that the velocity in the main flow is equal to the velocity in the capillary. For simulation of mixing this boundary condition is much easier to implement. The concentration of RhB in the tracer stream is set to 77mg/l.

3.2.2   Radial Dispersion by WMS

The postprocessing of the WMS data requires two calibrations. This makes the method more time intensive, however measurement data can still be collected very efficiently compared to the LIF method.

One calibration has to be done to compensate for the drift of the evaluation electronics with temperature. The same current I is not always converted to the same digital signal $\hat{I}$. This can be compensated by digitalizing a known current I and recording the digitalized signal $\hat{I}$. For this calibration the WMS is uncoupled from the A/D converter and a bank of resistors is put in place. For every receiver wire three different resistors are placed and the digital signal is recorded (Figure 3.8). This allows to make a linear fit of the
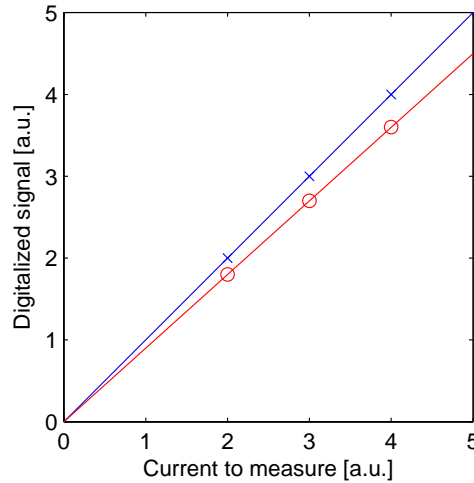
Figure 3.8: Drift of A/D with temperature. For every receiver wire a calibration is made with three known currents, allowing to estimate the characteristic of the A/D.

characteristic of the A/D converter.

$$\hat{I} = m \cdot I \tag{3.2}$$

This parameter m of the A/D converter is recorded after every measurement. The measurement data $\hat{I}$ is then divided by the slope m of the characteristic of the A/D to obtain the analog current I.

$$I = \frac{\hat{I}}{m} \tag{3.3}$$

Because of small manufacturing differences the nodes of the sensor do not impose the same resistance. Therefore a calibration of all nodes is done by measuring the conductivity of a known tracer concentration. The high calibration is done by placing a solution of concentration 0.175g/l into the measurement section, giving the upper calibration value I_{high} for every node of the sensor. The second calibration is made with deionized water giving the lower calibration value I_{low}. At low salt concentration the fact that the conductivity of the liquid is a linear function of the salt concentration can be used:

$$c(t) = \frac{I(t) - I_{low}}{I_{high} - I_{low}} \cdot c_{high} \qquad (3.4)$$

From this measurement data $C(t)$ which contains the concentration of 8×8 points during $10s$ measured with 1000Hz the temporal mean is calculated for every pixel. For the calculation of the CoV the nodes at the boundary were not included. The reason for this is that at the boundary the electric field is non-symmetric, making these measurements more sensitive to environmental disturbances. From this mean image the CoV calculated according to eq.(2.1).

Radial dispersion measurements are done with the WMS for flowrates from 100ml/min to 2500ml/min. KCl is used as tracer substance. The Schmidt number of this substance in water is $Sc = \nu/D_m = 527$. The selection of a tracer concentration has to fulfill the requirement that the tracer does not influence the flow. At too high salt concentration the solution becomes much heavier than the distilled water and gravitational effects can be observed. Therefore a the tracer concentration as low as possible has to be chosen. There is however also a lower limit for the tracer concentration because the noise becomes larger the lower the conductivity is. The tracer concentration of 17.5g/l is considered to be a good compromise. At this concentration the influence of gravity can be neglected. This is seen in an experiment of laminar flow through a horizontal empty pipe. In this experiment it is observed with the wire-mesh sensor that the tracer does no more tend to flow at the bottom of the pipe like it is the case at higher salt concentrations. The flowrate of the tracer solution is chosen to be 1 : 100 of the main flowrate, like in the LIF measurements with the straight injection capillary. With this choice of flowrate ratio the concentration of tracer in the

mixed condition is 0.175g/l. For injection of the tracer the straight injection capillary was used (Figure 3.7).

3.2.3   Axial Dispersion by WMS

RTD measurements are done with the wire-mesh sensor for determining the axial dispersion properties of an SLS foam structure. A standard electrode measures the concentration of a tracer in an extended control volume. In case of the WMS one measures the conductivity in 8×8 small control volumes. With this device it is intended to measure RTD in single and multi-phase flows. The high spatial and temporal resolution allows to use sophisticated post-processing algorithms. This has the intention to be able to filter out the influence that the bubbles have on the measurements.

Single-phase flow
For a proof of the concept the axial dispersion is measured in single-phase flow. A scheme of the setup for RTD measurements is shown in Figure 3.9. This setup contains an SLS foam as premixer which guarantees that the
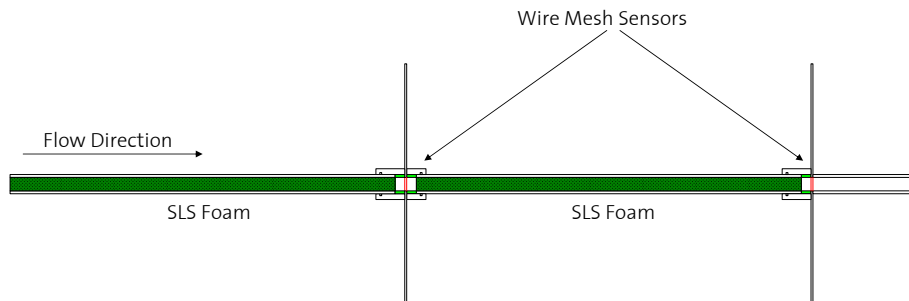
Figure 3.9: Setup for measuring RTD with two wire-mesh sensors. A premixer is used to ensure radial homogenization and establishing the flow.

tracer is equally distributed over the cross section. The second function of the premixer is to ensure the turbulent flow is developed. As shown in Section 4.2.1 the entrance flow situation affects also the dispersion coefficient. With the setup containing a premixer it is ensured that we do not measure in the entrance section of the packing.

For the generation of the pulse a six-way valve is used (Figure 3.10). A loop with a volume of 50µl is filled with 30g/l KCl solution. The flowrate through the valve is always set to 1 : 100 of the main flowrate.
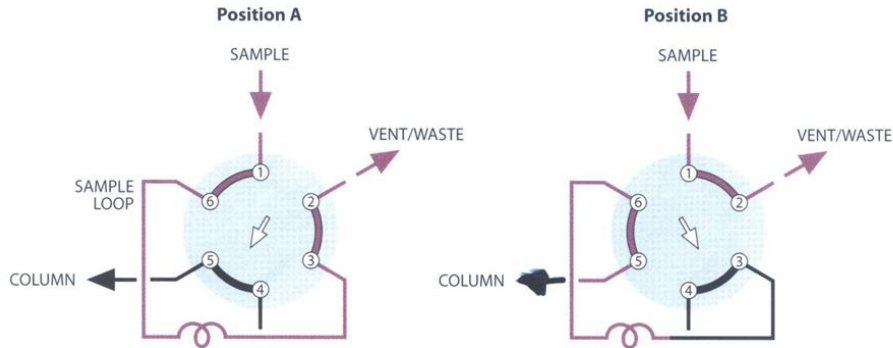
Figure 3.10: Six way valve used for injection of tracer pulse. Left: position
to fill loop. Right: position to inject pulse.

In the axial dispersion measurements it not required to make a calibra-
tion of the A/D converter after every measurement. The reason for this is
that in the axial dispersion measurements a calibration of the sensor can
very easily be done just before the experiment. If we do that we assume
that within the short time between calibration of the sensor at high concen-
tration and the measurement the characteristic of the A/D converter does
not change. Like this the concentration can simply be calculated from the
digital signals by:

$$c(t) = \frac{\hat{I}(t) - \hat{I}_{low}}{\hat{I}_{high} - \hat{I}_{low}} \cdot c_{high} \qquad (3.5)$$

What remains is to describe the postprocessing of the measurement data.
The measurement contains data for 8×8 pixels and, depending on the
flowrate, 25s to 2min duration resolved with 1kHz. This data is available
separately for both the inlet and the outlet sensor. First, the measurements
at the four boundary nodes are discarded, because they do not lie inside
the pipe cross-section. Then for every snapshot the average over the cross
section is calculated. It is then observed that the integration of the signals at
the inlet and the outlet over time are not exactly the same. For this reason
both signals are scaled such that the integral over time is unity. Finally the
procedure described in Section 2.2.3 is applied to calculate the RTD with
the dispersion model.

Multi-phase flow

Two-phase flow measurements are done in the bubbly flow regime. The gas is injected via a capillary right in front of the premixer as shown in Figure 3.11. The premixer is now used for an even radial distribution of tracer and to ensure the bubbles are dispersed already at the inlet sensor. The pulse of KCl tracer is injected further upstream ($\approx$ 1m).
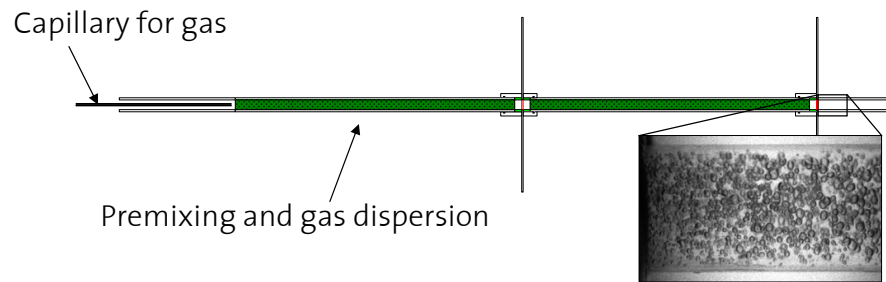
Figure 3.11: Setup for measurement of RTD in air-water two-phase flow. The gas is injected via a capillary just in front of the premixing structure. The photo of bubbles at the outlet show a good dispersion of the gas phase.

To interpret the measurements one has pay attention to what the WMS measures in a two phase flow. The intention is to measure the concentration of tracer in the liquid phase. In a single phase flow the concentration is linearly proportional to the conductivity. Also in a two-phase flow the conductivity of the liquid phase is proportional to the concentration of tracer in the liquid phase. However what the wire-mesh sensor measures is no more the conductivity of the liquid phase alone but a combination of the conductivity of the liquid phase and the conductivity of the gas phase. So if the WMS measures decreased conductivity it is unknown if this comes from a lower tracer concentration in the liquid or from a higher gas hold-up.

In a calibration experiment the conductivity of the liquid phase is set to a constant value by injecting tracer solution of 30g/l KCl in front of the premixer. It is assumed that the tracer is homogeneously distributed in radial and axial direction. This is justified by recalling that a structured foam premixer of 200mm length is installed, which radially distributes the tracer. The signal measured under this conditions for one outlet node is shown in Figure 3.12. The high frequency of the signal stems from the bubbles which pass the sensor in a very short time. Assuming no slip between the phases the time for a bubble to pass the sensor is less than 1ms for a
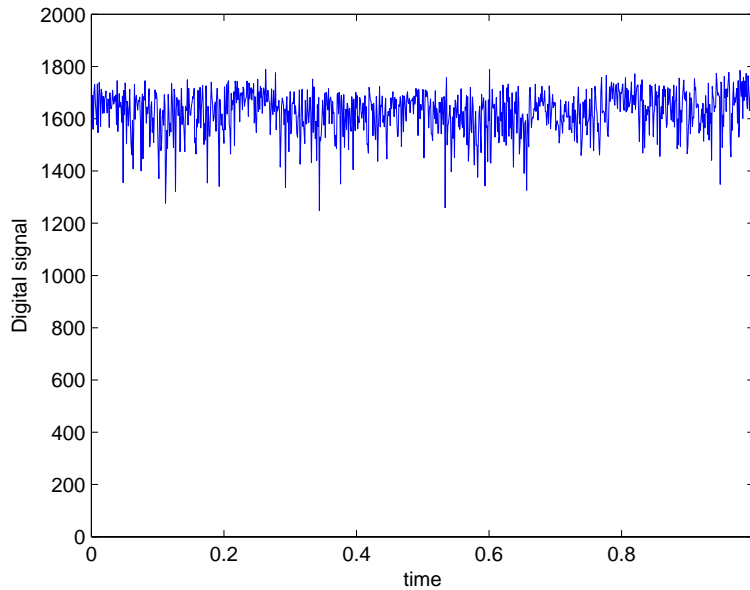
Figure 3.12: Calibration measurement with frequency of 1kHz of a two-phase flow with liquid flowrate of 1500ml/min and gas flowrate of 150ml/min. Continuous injection of tracer with concentration of 30g/l and flowrate of 15ml/min.

total flowrate of 1500ml/min. The idea to handle this high frequency signal is to consider the influence of the bubbles as constant in time. This means that still a linear characteristic between sensor signal and conductivity of the liquid phase is expected. The calibration of the sensor was then made similar to the calibration in the single phase experiment. The only difference being that now a twophase flow is measured.

$$c(t) = \frac{\hat{I}(t) - \hat{I}_{low}}{\hat{I}_{high} - \hat{I}_{low}} \cdot c_{high} \qquad (3.6)$$

where $\hat{I}_{high}$ and $\hat{I}_{low}$ are the calibration measurements with the same two-phase flow as in $\hat{I}(t)$. From this signal the postprocessing continues like in the single-phase experiments.

3.3   Plant Setup

The measurements of this thesis were carried out in a horizontal setup. Figure 3.13 shows the process flow diagram.
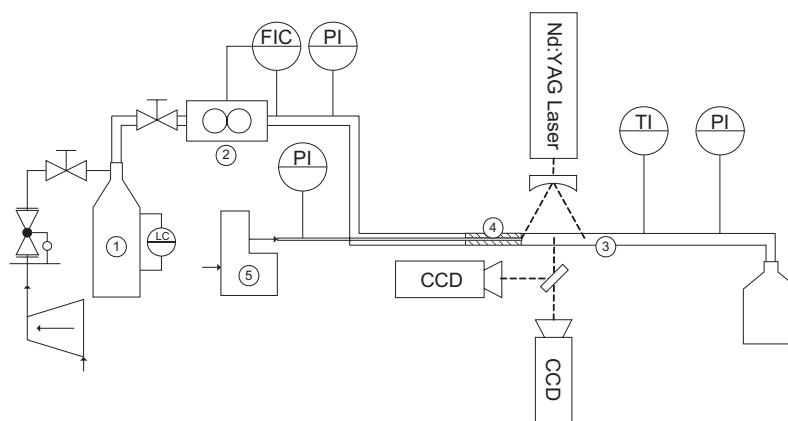
Figure 3.13: Flow chart of the experimental setup.

The deionized water for the measurements is supplied via a pressurized tank (Figure 3.14). With this configuration it is possible to control the liquid flowrate very accurately. The liquid flow controllers (Bronkhorst Hi-TecCORI-FLOW M55) shown in Figure 3.14 are installed below the tanks. For the gas flowrate control the pictured controllers are not used because of lack of documentation. For this reason it is decided to make a volumetric measurement of the gas flowrate with a measuring cylinder.

As an example of a measurement setup Figure 3.15 shows a picture of the wire-mesh sensor mounted for RTD measurements.

3.4   Investigated Packings

Two manufacturing techniques are used for the packings investigated in this thesis. The plastic packings have the advantage that they are optically accessible, which is required for LIF measurements.

3.4.1   Selective Laser Sintering

Metal structured foam packings of 200mm length were fabricated by Selective Laser Sintering (SLS). SLS is an additive manufacturing technique that
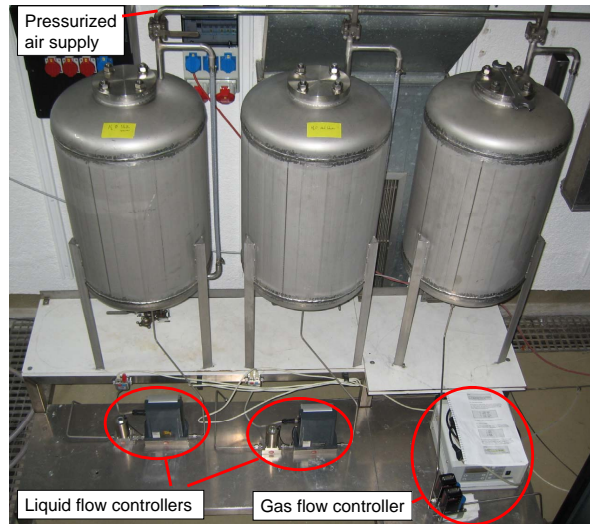
Figure 3.14: Two pressurized vessels for liquids (mains water and deionized water) and one vessel for pressurized air.
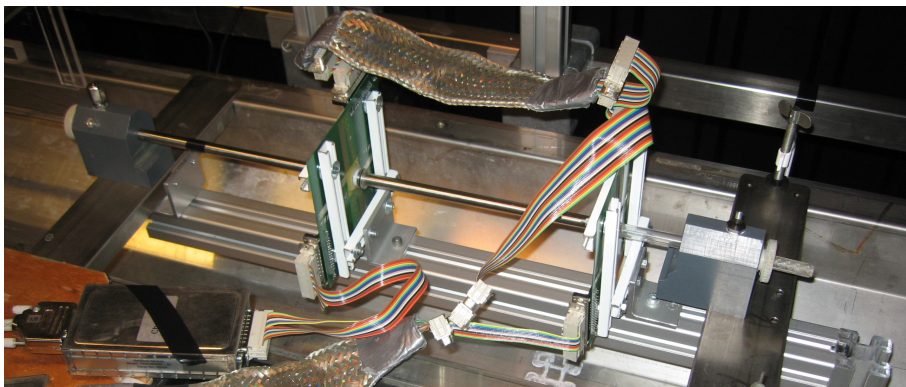
Figure 3.15: WMS mounted for multi-phase RTD measurements.

sinters metal particles by the use of a laser. With this technique, geometries of arbitrary shape can be produced. A further advantage is that it leaves a very high surface roughness (Figure 3.16) which is advantageous for catalyst deposition. The parts were produced by Ecoparts, Rüti ZH.
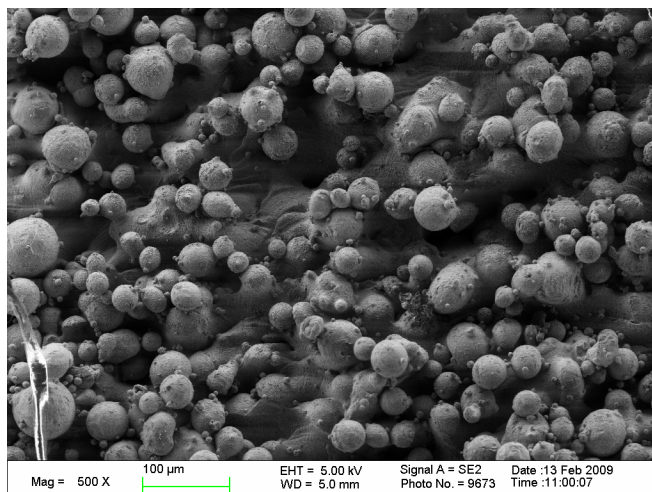
Figure 3.16: Surface of a structure produced by SLS. The raw material is still visible, giving the structure a high roughness and by that a high specific surface.

3.4.2   Stereolithography

The foam geometry is produced in plastic for the LIF experiments . For comparison and as benchmark for the structured foam also other packings were produced. The plastic packings were manufactured by Stereo lithography by VONALLMEN AG, Pfäffikon ZH. Stereo lithography is a manufacturing technique known from rapid prototyping and rapid manufacturing respectively. In a bath of liquid photopolymer a UV beam is used to selectively solidify the pattern given by a CAD model.

The CAD models are shown in Figure 3.17. The packings have a length of approximately 50mm and an inner diameter of 7mm. Every structure has a certain distance after which the geometry is repeated. It was then decided to take as many repetitions of the geometry to have approximately 50mm length. The exact length of the packings is given in table 3.1. The investigated foam is longer because it is from an earlier purchase. The struc-
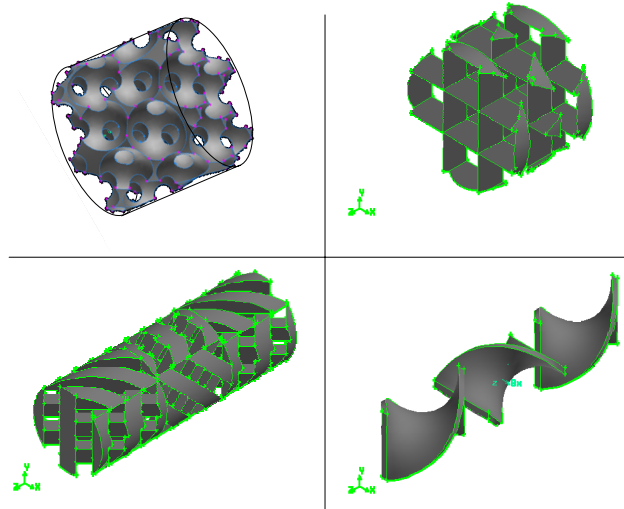
Figure 3.17: Packings produced by stereolithography. Top left: Structured foam (Inverse fixed bed). Top right: Triangular ligaments . Bottom left: Sulzer SMX. Bottom right: Kenics KM.

Table 3.1: Length of investigated packings.

Packing name	Length [mm]
Structured Foam	54.4
Triangular Ligaments	48.1
Sulzer SMX model	46.8
Kenics KM model	49.4

tured foam of the new purchase does not reproduce the CAD model very precisely. The reason for this is that the company changed the manufacturing process what made the ligaments of the foam become very thin, much thinner than in the CAD model and in the packing of the first purchase. It was already found before by Bäriswyl[41], that the ligament shape has a very strong effect on the flow field. For this reason it was decided to not further investigate the structured foam from the new purchase.

Chapter 4

Results and Discussion

4.1 Radial Dispersion

Radial dispersion is measured with LIF and a WMS. The first two sections of the results on radial dispersion present the LIF experiments. The third section contains the measurements with the wire-mesh sensor.

4.1.1 LIF with Side Injection Capillary

For enabling a comparison of the structured foam with the measurements that were already made for unstructured foams, LIF measurements with the side injection capillary are performed. The measured CoV as a function of the empty pipe Reynolds number is shown in Figure 4.1.

Comparing the four geometries it is observed that the Kenics KM structure mixes better than the others for all flowrates. The worst radial mixing performance is observed in the structure with triangular ligaments. On the pictures included in the graph of Figure 4.1 it is shown that even the worst of the investigated structures exhibit a good mixing performance.

The trend with increasing Reynolds number shows that mixing performance increases. However that trend is not very clear and there is quite some scattering in the results. One explanation for the scattering is that the boundary conditions change with the flowrate. At low flowrate the side injection capillary spreads the tracer over the cross-section already at the inlet of the packing. At higher flowrates the tracer is not spread over the whole cross-section as shown in Figure 4.1. With the straight injection capillary we have observed much less scattered results.
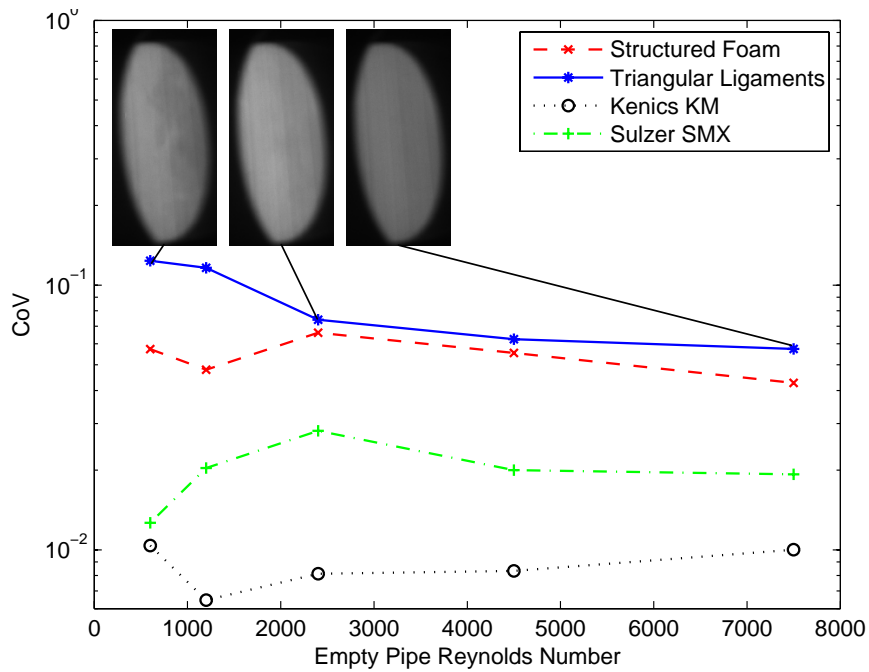
Figure 4.1: CoV as a function of empty pipe Reynolds number measured by LIF in a setup with side injection capillary.

4.1.2 LIF with Straight Injection Capillary

To have the same boundary condition for tracer distribution at the inlet independent of the flowrate a measurement campaign with a straight injection capillary is made. Sample images of these measurements are collected in the Appendix A. The resulting CoV from these images is plotted in Figure 4.2. We observe much less scattering than in the measurements with the side injection capillary.

The values of the measured CoV range from 0.345 to 0.0096. From a calibration experiment the CoV of a homogeneous distribution is known to be 0.008.

It is observed that the Sulzer SMX shows a good mixing performance already at very low flowrates. The other investigated packings show worse mixing performance at the lowest flowrate. The reason why the Sulzer structure is better at low flowrates is that it is a laminar mixer. At the lowest flowrate we have predominantly laminar flow in all structures. In a laminar flow through the Kenics mixer the tracer only sees very few lamination steps. In a structured foam there are more lamination steps, i.e. from cell to cell,
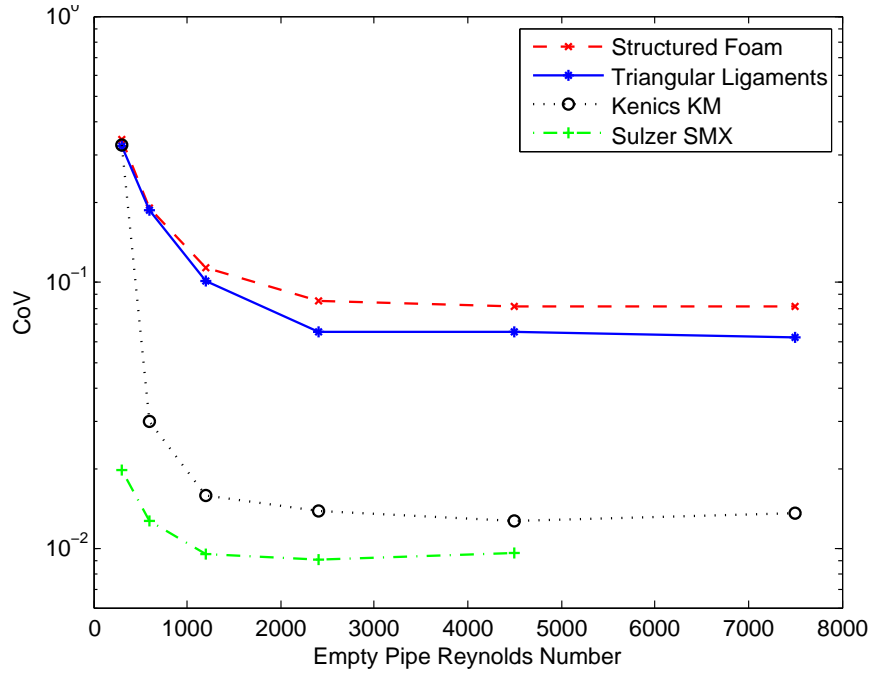
Figure 4.2: CoV as a function of empty pipe Reynolds number measured by LIF in a setup with straight injection capillary.

but the tracer separated by one ligament can recombine in a cell further downstream. Similar considerations hold for the structure with triangular ligaments. In the Sulzer structure however the lamination effect is much more pronounced. A fluid element that is separated by a strut of the packing is spread over the whole cross-section. This prevents that the separated fluid element can recombine further downstream.

The transition from laminar to turbulent regime occurs between the measurement at $Re = 300$ and $Re = 600$. In the turbulent region the mixing performance becomes better for all geometries. With higher Reynolds number the turbulent kinetic energy increases. This leads to a better mixing of the tracer over the cross-section by turbulence. A counteractive effect is that with increasing Reynolds number the mean residence time becomes smaller. An explanation why the CoV reaches a constant value for high Re could be that the effects of increased turbulence and decreased time for mixing balance out.

Contrary to the other structures the Sulzer SMX shows a small increase in CoV with Reynolds number. This means that at lower flowrate the mixing

performance is better. What we have to mention is that we did not measure the point at $Re = 7500$[1]. Scanning the literature in this direction, it was found that also Hobbs[4] observed best mixing performance (of a Kenics mixer) at low flowrates. His explanation for decreased mixing performance at higher Reynolds number is that regular islands develop in the flow, which present a barrier to uniform mixing. Wadley[24] observed decreasing performance with increasing Reynolds number in the turbulent regime of a Kenics KM. He assigns this behaviour to an artifact of feed distribution problems rather than to some intrinsic behaviour of the mixer itself.

Our attempt to explain why the Sulzer mixer could perform better at low flowrates is shown in Figure 4.3. The idea behind this hypothesis is that the
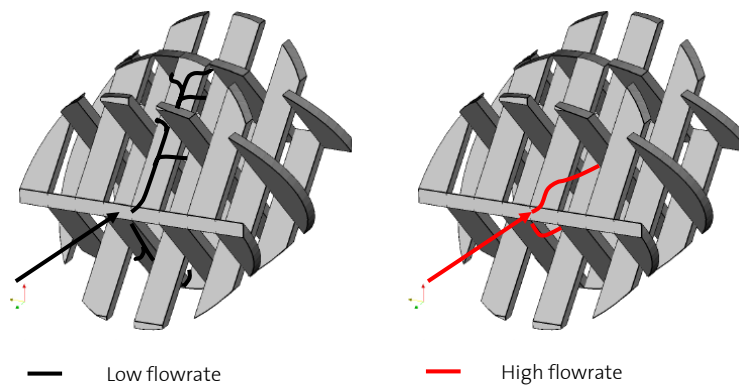
Figure 4.3: Possible explanation for better mixing of Sulzer structure at low flowrate. At low flowrate more transport in boundary layer on structure. At higher flowrate boundary layer is thinner, less substance can be transported along ligaments.

Sulzer mixer is a laminar mixer already showing good mixing performance at low flowrates. At low flowrates lamination of the flow is the main mechanism of mixing. When a tracer substance arrives at the packing it is divided into two streams (left image in Figure 4.3). These two streams then travel in the direction of the ligaments and eventually are spread over the whole cross-section. When leaving the ligament and flowing further downstream the fluid elements are again separated but now in the perpendicular direction.

---

[1]Sulzer mixer shows the highest pressure drop. At the high flowrate it is not possible to inject with the syringe the required 25ml/min. The same measurement with the wire-mesh sensor is not a problem as a smaller syringe (20ml) can be which is able to inject 25ml/min. For the LIF measurements however it is not possible to take a smaller syringe because the measurements last for more than one minute.

When analyzing the flow field at higher Reynolds numbers this lamination effect is reduced. From fluid dynamics it is known that the boundary layer becomes thinner with increasing Reynolds number. This implies that there is less transport along the ligaments with increasing Reynolds number. Unfortunately the significance of the increase in CoV is very low, what makes is hard to draw a final conclusion. One way of assessing this is to measure with LIF the radial mixing performance of a short Sulzer SMX with only two to four elements. In such an experiment the segregation could be measured much more accurately.

A further observation is that the industrially applied mixers[2] show a better radial mixing performance than our geometries. For the Sulzer mixer this was expected because it has a very strong lamination of the flow by ligaments spanning the whole cross-section. In the structured foam the lamination effect does not spread fluid elements over the whole cross section but only from one cell into the downstream cells. From these downstream cells the flow is recombined in a cell further downstream. The mixing performance of our structured foam geometry could therefore be improved by avoiding that a flow separated by a ligament is recombined in the next cell. This could be achieved by selectively closing some of the pores of our structure.

An unexpected observation is that the Kenics mixer outperforms both of our self-designed structures. Looking at the CAD models of Figure 3.17 one sees that in the Kenics mixer the flow can basically flow free from one end of the cross-section to the other. In our designs this is not the case and the largest eddies in the structured foam are smaller than the pore size. In the Kenics however there can be large eddies in the size of the cross-section, transporting the tracer over the whole cross-section.
What has to be mentioned is that we measure only the macromixing. With the resolution of our measurement method, which is 0.06mm for LIF, we only observe mixing phenomena down to this scale. In industrial applications, for example for chemical reactions, it is important to also have a good micromixing performance. Because of the low pressure drop of the Kenics mixer we expect much less turbulence at the micro scale and therefore less micromixing in this mixer. Another drawback of the Kenics KM mixer is that it has a very low specific surface, which is a major drawback in some

---

[2]Industrial mixers: Kenics and Sulzer. Own design: structured foam and triangular ligaments.

applications. In summary we conclude that choosing a mixer is not a general question but is case dependent.

Accounting for the pressure drop:

To qualify static mixers according their radial mixing performance it is probably not a good approach to compare static mixers of 50mm length. One mixer with a high pressure drop could mix well, while a second has a very low pressure drop with bad mixing performance. If however one would compare mixers having equal pressure drop the second mixer could be better. One approach of considering the pressure drop is by multiplying the CoV by the friction factor f. The Fanning friction factor was used, which is calculated according to equation (4.7).

The resulting curves are shown in Figure 4.4. The Sulzer mixer having the highest pressure drop becomes worse in this graph. As the Kenics KM mixer has a very low friction factor this will dominate in this graph.
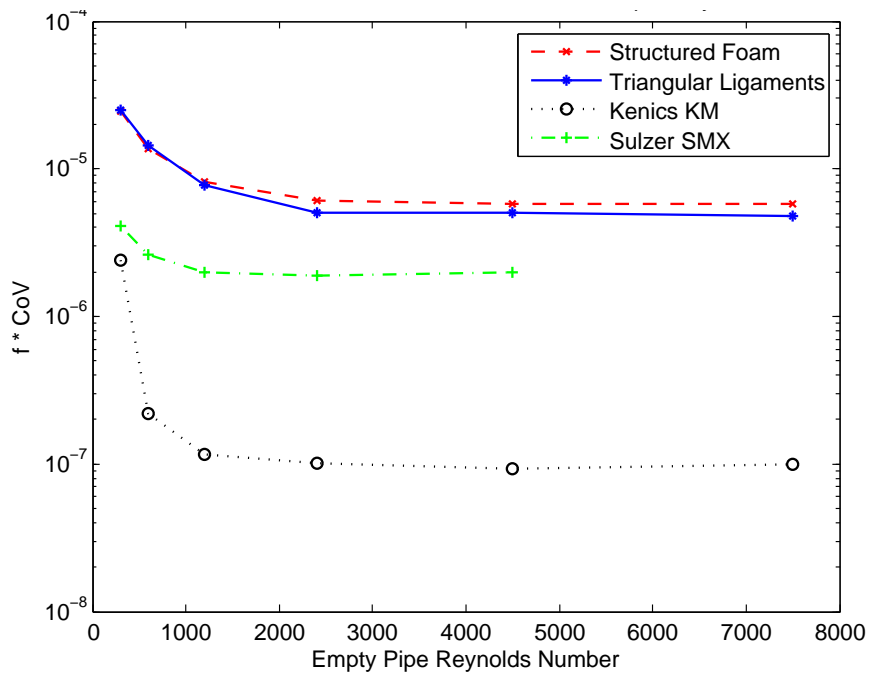
Figure 4.4: CoV multiplied by friction factor as a function of empty pipe Reynolds number measured by LIF in a setup with straight injection capillary.

Also this graph is not very satisfactory. Unfortunately it is not clear whether one prefers to have a ten times lower CoV or to have a ten times

lower friction factor. Another way of comparing different packings could be to investigate the mixing behaviour of packings with equal pressure drop. By that however one changes also all other parameters like mean residence time, specific surface, etc. Therefore we conclude that it is also meaningful to compare mixers of the same length as discussed above.

4.1.3   WMS with Straight Injection Capillary

One of the objectives of this thesis is to compare radial mixing measurements done with LIF to measurements with the wire-mesh sensor. It was decided to use the straight injection capillary for the WMS measurements. The coefficient of variation as a function of empty pipe Reynolds number is shown in Figure 4.5. What can be observed is again that the Sulzer mixer shows a good performance already at the lowest flowrate. The other geometries show a worse mixing performance at the lowest flowrate, which is then increasing with higher Reynolds number. What we also observe is that the industrial mixers are slightly better.
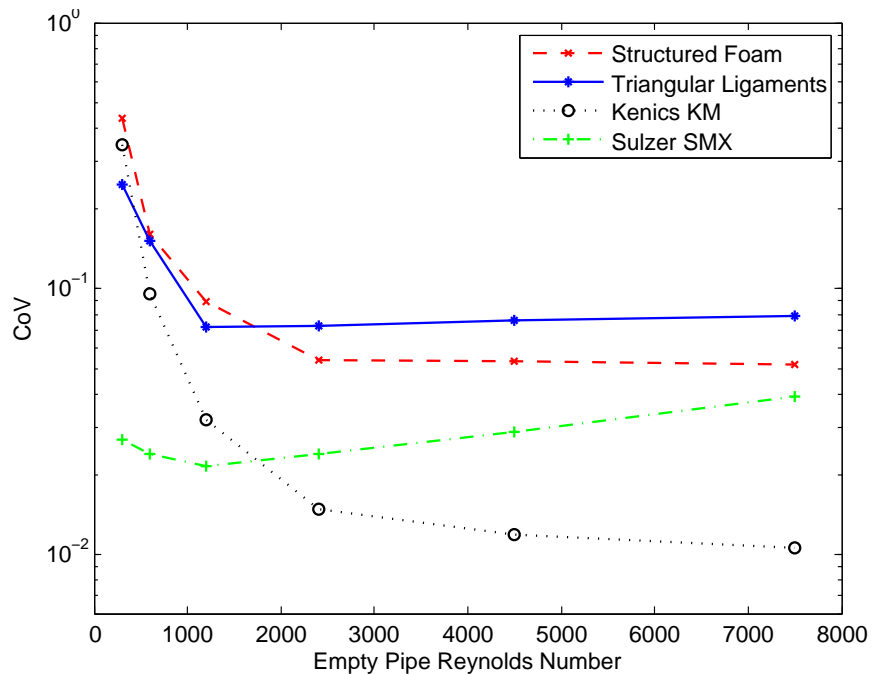
Figure 4.5: CoV as a function of empty pipe Reynolds number measured by wire-mesh sensor in a setup with straight injection capillary.

Comparison WMS - LIF

Now comparing the measurements with the wire-mesh sensor to the measurements done with LIF we do not see a perfect match of the two methods. One disagreement is that in the measurements with the wire-mesh sensor the structured foam mixes better than the packing with triangular ligaments. In the LIF experiments it is the opposite.

Another disagreement is that with the WMS we observe a more pronounced decrease of mixing performance of the Sulzer SMX. This is not observed in this extent in the LIF experiments, where only a small increase in CoV can be identified. What has to be mentioned is that the coefficient of variation is plotted on a logarithmic scale in Figure 4.5. This amplifies the increase in CoV, which is only from 0.024 to 0.040.

In general, LIF is more trusted because it is a well-known and broadly accepted measurement technique for radial mixing. In contrast to that this is the first time that a wire-mesh sensor is used to measure radial mixing. Observing different measurement results we need to remind us that the measurement principles are very different, as summarized in Table 4.1. One

Table 4.1: Comparison of LIF and WMS.

LIF - Laser Induced Fluorescence	WMS - Wire Mesh Sensor
Non-intrusive	Intrusive
High spatial resolution of 0.06mm	Low spatial resolution of 1mm
Low temporal resolution of 4Hz	High temporal resolution of 10kHz
Time consuming and expensive	Simple and fast
Well established technique	Only known for special applications
Optical access required	No optical access required

of the major differences of the two measurement techniques is the spatial resolution. From the images in the Appendix it is seen that structures resolved by LIF are not seen by the wire-mesh sensor. This could lead to different estimates of the CoV and also to different trends with Reynolds number.

We conclude therefore that the wire-mesh sensor is not the measurement method of choice for radial mixing.

4.2 Axial Dispersion

Axial dispersion experiments are made in a metal SLS foam of 0.2m length. When measuring with different premixers it is observed that the estimated axial dispersion coefficient is not equal (Figure 4.6). Without premixer the dispersion coefficient is estimated to be four times lower than in the case with a Sulzer SMX as premixer.
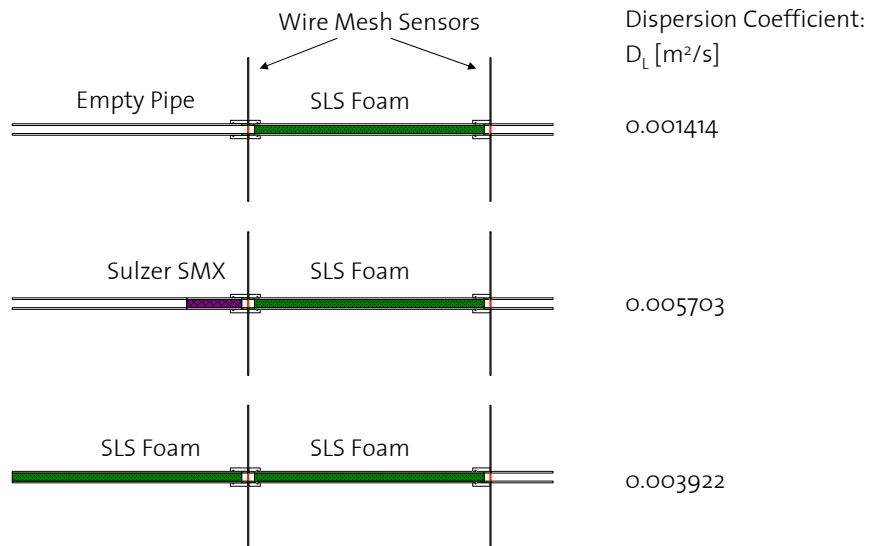
Figure 4.6: Estimated dispersion coefficients with different premixers at empty pipe Reynolds number $Re = 4500$. The highest dispersion coefficient is measured with a Sulzer SMX as premixer, which creates highly turbulent flow at the entrance of the measurement section. With the empty pipe the turbulence in the entrance of the measurement section is minimal leading to the smallest dispersion coefficient.

From literature it is known that the dispersion coefficient of an investigated structure is a function of the length. Han [1] observed this in packed beds, Paine [3] in capillary tubes and Delgado [2] has a section about the effect of column length in his review paper. The explanation in literature why dispersion coefficients are a function of the length are however not satisfying. Our attempt is to describe this with the theory about entrance length.

4.2.1   Hydrodynamic Entrance Length

For a flow in an empty pipe it needs a certain length until the flow has developed.

$$El_{laminar} = \frac{L_{entrance}}{d} = 0.06 \cdot Re \qquad (4.1)$$

$$El_{turbulent} = \frac{L_{entrance}}{d} = 4.4 \cdot Re^{1/6} \qquad (4.2)$$

Developed flow in the laminar case means that the velocity profile reached its characteristic shape. In a turbulent case developed flow means that the turbulent length scale distribution has developed. With the modern measurement techniques of today it is possible to measure the distribution of eddy sizes in a flow very detailed (Pope[35]). The distribution of large scale eddies is determined by the solid structure through which the fluid flows. Small scale eddy size distribution down to the Kolmogorov length scale follow similar profiles for all flows independent of geometry. When analyzing a flow from an empty pipe into a packing the packing will introduce large-scale eddies to the fluid. These large scale eddies transfer their energy to smaller eddies. The length of packing it needs to reach a steady state where the distribution of eddy sizes does not change anymore is the entrance length. This entrance length for the turbulence is also the entrance length of the axial dispersion coefficient. Figure 4.7 shows qualitatively the evolution of turbulence and dispersion coefficient in the entrance section of a packing.

Within this thesis the entrance length in our packings is not measured. An estimate is made by comparing it to literature data. Eq. (4.2) tells us that in turbulent flow the entrance length in an empty pipe is more than ten times the diameter of the pipe. Mokrani[25] measured axial evolution of turbulence intensity. He found that in his system of 20mm diameter the flow is established after 130mm, which is 6.5 times the diameter.
Our approach to circumvent the entrance behaviour is to use a premixer for establishing the flow as shown in Figure 3.9 of the experimental section. The length of the premixer is 28 times the diameter, what is considered as being long enough for the flow to establish.
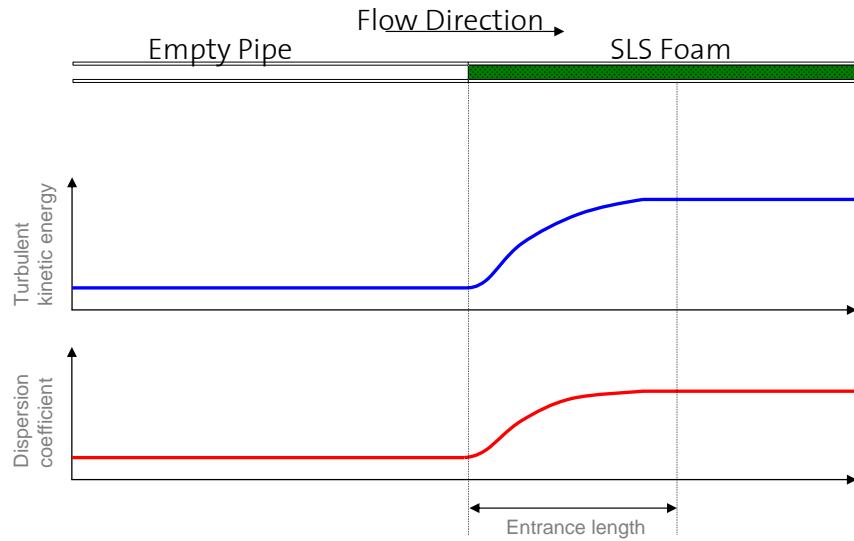
Figure 4.7: Qualitative evolution of turbulent kinetic energy and dispersion coefficient at the entrance of a packing.

4.2.2   Single Phase Axial Dispersion

Single phase axial dispersion in a 0.2m SLS foam was already measured by Zenklusen[43] with standard plate electrodes. Further he measured in unstructured foams of 0.2m and 1m length. He found that the dispersion coefficients in the long packing are higher than in the short packing. This agrees with the discussion in Section 4.2.1. The entrance section, which has a low dispersion coefficient, has a much stronger influence in the measurements of the short packing.

For proving the concept of measuring axial dispersion with a wire-mesh sensor we first measure in a single-phase flow. Figure 4.8 shows the mean residence time of the measurements over the theoretically expected mean residence time according to eq. (2.2).

If there would be dead zones in the reactor through which the fluid does not flow, the measured mean residence time would be lower than the expected. The good agreement between the expected and measured values lead to the conclusion that there are no dead zones in the structure. At the lowest flowrate the measured mean residence time is lower than the expected. This is assigned to the inaccuracy of the mass flow controller at the lowest flowrate.

In Figure 4.9 the estimated dispersion coefficients are plotted over the
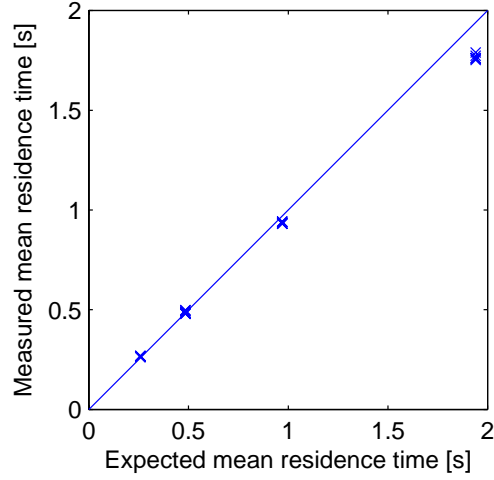
Figure 4.8: Theoretically expected and measured mean residence time.

pore Reynolds number.

The pore Reynolds number is defined as:

$$Re_{pore} = \frac{u \cdot d_{pore}}{\nu} \tag{4.3}$$

where $u = v/\epsilon$ is the interstitial velocity and $d_{pore} = 0.92$mm is the pore diameter. At every investigated flowrate five pulse experiments are made. The results show that the experiments are repeatable. Two exceptions are observed in the measurements with $Re_{pore} = 379$ which can be qualified as outliers. The reason why these two measurements show a lower dispersion coefficient can not be identified. For the other three measurements the standard deviation is 11%, 6% and 4%.

It is observed that the dispersion coefficient increases with increasing Reynolds number. This is explained by the increased turbulence of the flow which leads to more axial dispersion.

In an experiment with very low velocity the dispersion coefficient is expected to be equal to the diffusion coefficient because there is no turbulence. This implies that the curve in Figure 4.9 crosses the y-axis at $D_L = D_m$. The molecular diffusion coefficient of KCl in water is known to be $D_m = 1.9 \cdot 10^{-9}$, which is much smaller than the dispersion coefficient in this experiments, i.e. 10^6 times smaller. This motivates not to take an offset for the fit of the power law. The estimated coefficients of the power law show that the
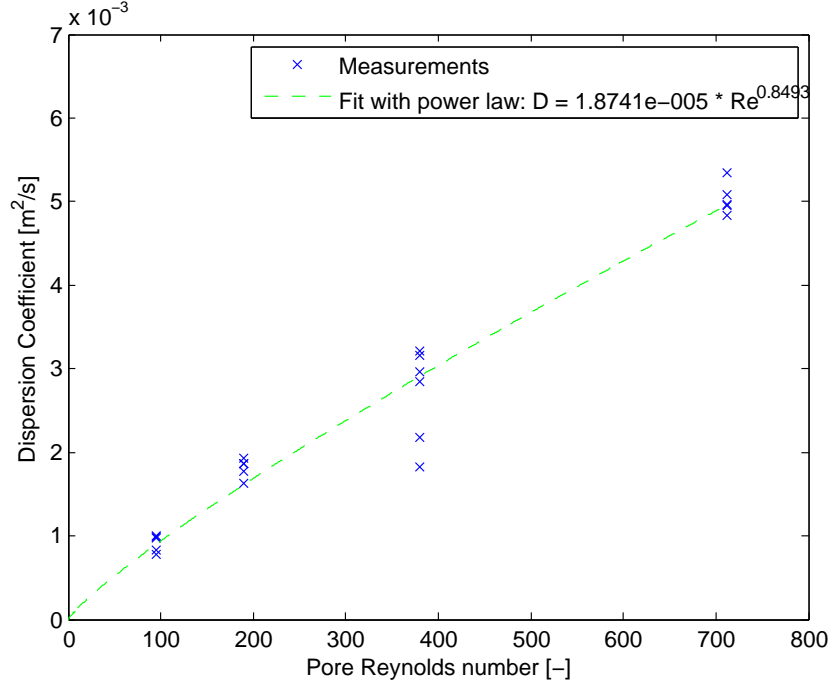
Figure 4.9: Dispersion coefficient as a function of pore Reynolds number measured in a SLS foam of 0.2m length.

dispersion coefficient increases with Re_{pore} to the power of 0.85.

The measurements are also compared to the ones by Zenklusen[43] and to other data from literature, that was collected by Han[1]. Figure 4.10 shows on the x-axis the pore Peclet number, which is defined as:

$$Pe_{pore} = \frac{u \cdot d_{pore}}{D_m} \tag{4.4}$$

The y-axis shows the axial dispersion coefficient scaled by the molecular diffusion coefficient.

In Figure 4.10 the measurements of this thesis are labeled as *SLS WMS*. The measurements of a 0.2m SLS foam by Zenklusen I are labeled *SLS L=0.2m*. It can be seen that our estimated dispersion coefficients are higher. The reason for this is that we do not have the entrance section in our measurement section.

We also compare our measurements to data of different packings collected by Han[1]. Han shows that in a log-log graph the dispersion coefficient in-
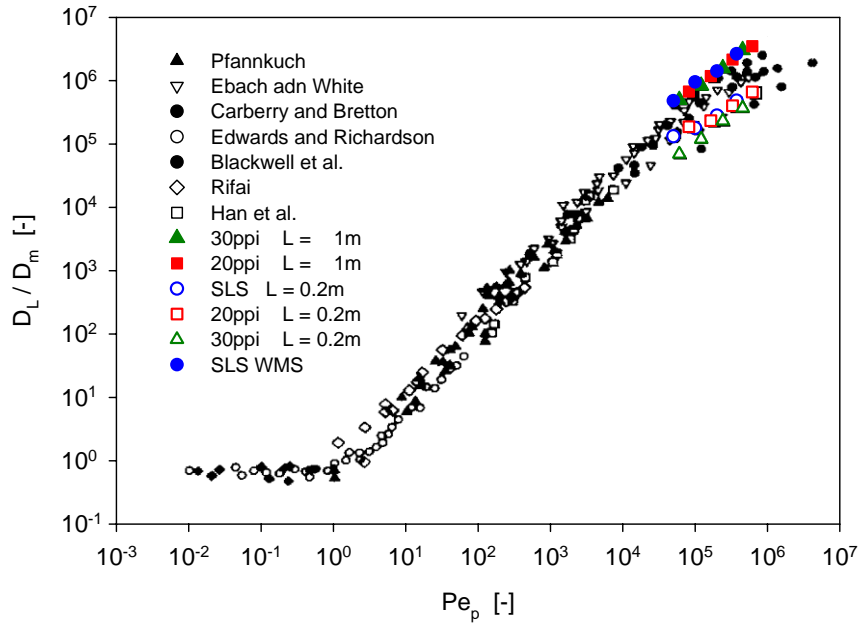
Figure 4.10: Comparison of measurements within this thesis (SLS WMS) to previous measurements and data from literature [1].

creases approximately linear with pore Peclet number. At very low Peclet numbers a constant value of the dispersion coefficient, i.e. $D_L/D_m = 1$ can be observed. This means that at very low Peclet number there is no dispersion by turbulence but only by diffusion. Our measurements lie in the upper range of Peclet numbers. We observe that our estimated dispersion coefficient lies at the upper limit of the measurements shown by Han. Interestingly there seams to be a range in which all different kinds of packings lie, including the ones investigated in this thesis.

Choosing the best flowrate of a reactor

Designing a tubular reactor one has to decide whether to take a low or a high flowrate. As the measurements show a higher dispersion coefficient with higher Reynolds number one could think that a reactor with low flowrate shows a better plug-flow behaviour. That this is not the case is shown in Table 4.2, that lists a comparison of two reactors where in one of them the flowrate is by a factor of f times higher.

When the velocity is scaled with the factor f, also the length has to be scaled with f in order to keep the mean residence time equal. The

Table 4.2: Comparison of reactor with high flowrate to reactor with low flowrate. Scaling factor f.

	Low flowrate	High flowrate
Interstitial velocity	u_0	$u_1 = f \cdot u_0$
Length of reactor	L_0	$L_1 = f \cdot L_0$
Mean residence time	τ_0	$\tau_1 = \tau_0$
Axial dispersion coefficient	D_0	$D_1 = \left(\frac{u_1}{u_0}\right)^{0.85} \cdot D_0 = f^{0.85} \cdot D_0$
Vessel dispersion number	$\frac{D_0}{u_0 \cdot L_0}$	$\frac{D_1}{u_1 \cdot L_1} = \frac{f^{0.85} \cdot D_0}{f u_0 \cdot f L_0} = f^{-1.15} \cdot \frac{D_0}{u_0 \cdot L_0}$
Pressure drop (assuming constant λ)	$dP_0 = \frac{\rho}{2}\frac{\lambda L_0}{d}u_0^2$	$dP_1 = \frac{\rho}{2}\frac{\lambda f L_0}{d}\left(f u_0\right)^2 = f^3 \cdot dP_0$
Throughput	$\dot{m}_0$	$\dot{m}_1 = f \cdot \dot{m}_0$

mean residence time is given by the reaction and can not be adjusted. From Figure 4.9 it is known how the dispersion coefficient scales with velocity. For determining the width of the residence time distribution the vessel dispersion number has to be calculated, which is found to decrease with the scaling factor as $f^{-1.15}$. As described in Section 2.2.2 a low vessel dispersion number represents a narrow residence time distribution. This is an interesting result telling that to obtain a plug flow reactor a high factor of f should be taken. On the other hand the pressure drop and investment costs for the reactor increase. In the end there is a tradeoff between narrow RTD and other parameters. For this reason a different flowrate is found to be the optimum for different cases.

4.2.3 Multi Phase Axial Dispersion

As an example of a measurement signals in a two-phase flow Figure 4.11 shows the signals at the inlet and outlet after the postprocessing described in Section (3.2.3).
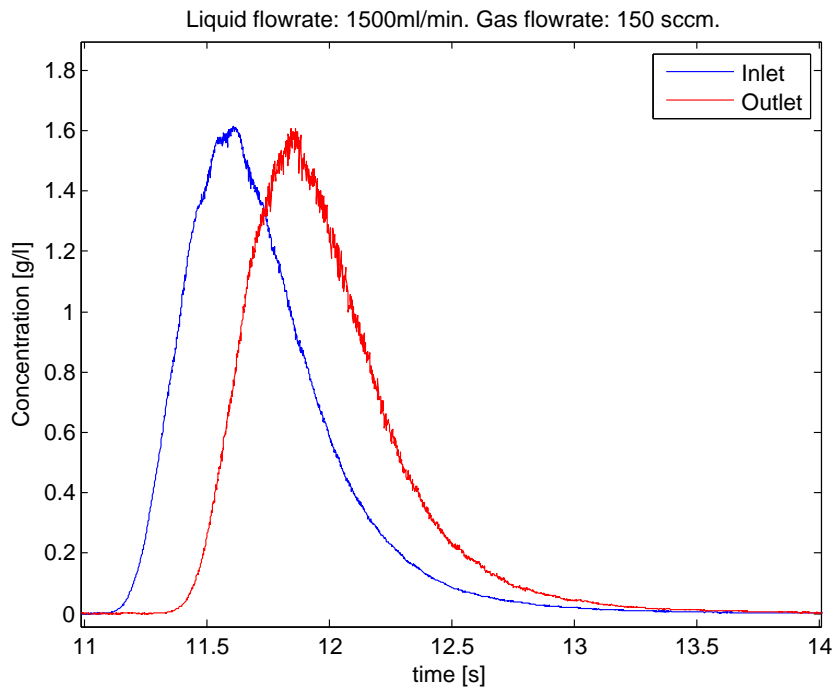
Figure 4.11: Measured concentration peaks at inlet and outlet as average over 8×8 measurement points. At the outlet the gas flowrate is higher because the pressure is lower. This leads in general to a more noisy signal at the outlet.

It is observed that the signal at the outlet is more noisy than at the inlet. The signal to noise ratio at the inlet is around 80 while at the outlet it is approximately 30. The reason for this is that at the outlet the volumetric gas flowrate is higher because the pressure is lower. However the measured pulses show much less noise than measurements with standard electrodes. This is according to our expectations as we measure at 8×8 points. With our approach to determine $E(t)$ it would not be a problem to even treat more noisy signals.

Multi-phase axial dispersion was measured at liquid flowrates of 800ml/min and 1500ml/min with different gas flowrates. The estimated dispersion co-

efficients when the liquid flowrate is 800ml/min are shown in Figure 4.12.

Figure 4.12: Estimated axial dispersion coefficients as a function of gas flowrate with constant liquid flowrate of 800ml/min.

The gas flowrate in sccm is plotted on the x-axis. The volumetric transport fraction of the gas can be calculated from the gas and the liquid flowrates:

$$\dot{\epsilon}_{gas} = \frac{\dot{V}_{gas}}{\dot{V}_{gas} + \dot{V}_{liquid}} \tag{4.5}$$

That tells us that the investigated range of volumetric transport fractions is from 0% to 42%.

For every investigated flowrate three pulse experiments were made. At some flowrates we observe high standard deviation of the results. It is not clear if this is a problem of the measurement technique or if this is the physical behaviour of the two-phase flow. Drawing a trendline with linear regression for this data it is observed that dispersion coefficients increase with higher gas flowrate.

The results for the liquid flowrate of 1500ml/min are shown in Figure 4.13. Again the gas flowrate in sccm is on the x-axis. Now the volumetric transport fraction reaches from 0% to 12%. In this measurement series only
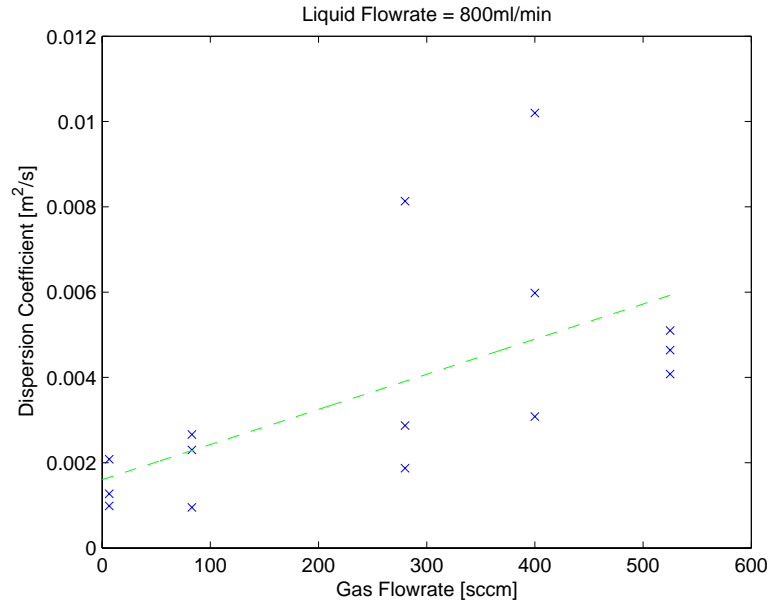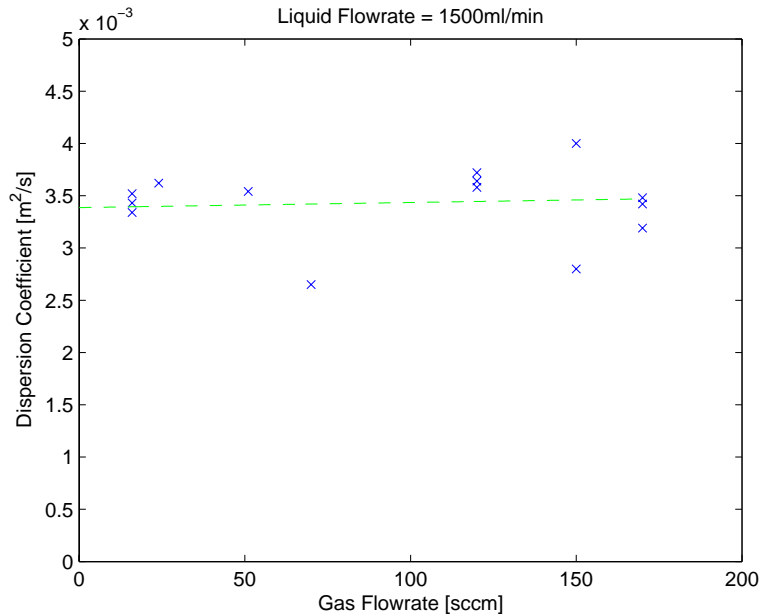
Figure 4.13: Estimated axial dispersion coefficients as a function of gas flowrate with constant liquid flowrate of 1500ml/min.

one pulse experiment was made per volumetric gas flowrate. Exceptions are the points at $\dot{V}_{gas} = 16$, 120 and 170sccm. At these gas flowrates three pulse experiments were made. It is observed that the scattering of the estimated dispersion coefficients is lower than in the measurements of Figure 4.12. Drawing a trendline with linear regression we find that dispersion coefficients slightly increase with increasing gas flowrate.

Unfortunately it is not so easy to identify the mechanisms which change the dispersion coefficient. In the experiments the only parameter that is varied is the volumetric gas flowrate in sccm. What is expected is that a higher gas flowrate leads to more turbulence and by that to a higher dispersion coefficient. However by increasing the volumetric gas flowrate also the pressure drop over the packing increases. By this we observe at the inlet a higher pressure. Because the gas is compressible, the volumetric transport fraction of the gas at the inlet becomes lower. What also changes with changing gas flowrate is the frequency of injected bubbles. Because the capillary used for gas injection produces bubbles of a certain size, the time between two injected bubbles changes. By that there could be an additional frequency in the measurement signal that stems from the non-constant gas

flowrate.

In the single-phase measurements the data showed very low scattering and attempts to achieve this also in multi-phase measurements should be discussed. One idea of reducing the scattering of the results is to find an algorithm which identifies the bubbles and tries to only take the measurement values where there are no bubbles. Assuming no slip between the phases it can be calculated that at a liquid flowrate of 1500ml/min a bubble passes the wire-mesh sensor in less than 1μs. Because pulse experiments were done with a frequency of only 1kHz the single bubbles can not be resolved. A test measurement with a frequency of 10kHz is therefore made. Figure 4.14 shows such a signal for one node at the outlet sensor with constant concentration of tracer in the liquid phase.

Figure 4.14: Measurement with 10kHz. Concentration as a function of time for one node of the outlet sensor at liquid flowrate 1500ml/min and gas flowrate 108sccm. Constant tracer concentration.

Also from the signal measured with 10kHz the single bubbles can not easily be identified. In usual applications of the wire-mesh sensor the bubble size of the investigated two-phase flow is larger than the resolution of the sensor. In that case the conductivity in a node goes to zero when a bubble passes. When there is no bubble present in the node the signal has a constant high value. In our case however the bubbles are much smaller and have a

small impact which is of a very high frequency. Between two bubbles there is no time when we can identify a measurement signal that has a constant value, which could be assigned to the conductivity of the liquid phase. This makes it difficult to filter out the influence of the bubbles. Figure 4.15 shows a signal measured with 1kHz at one outlet node in a pulse experiment.
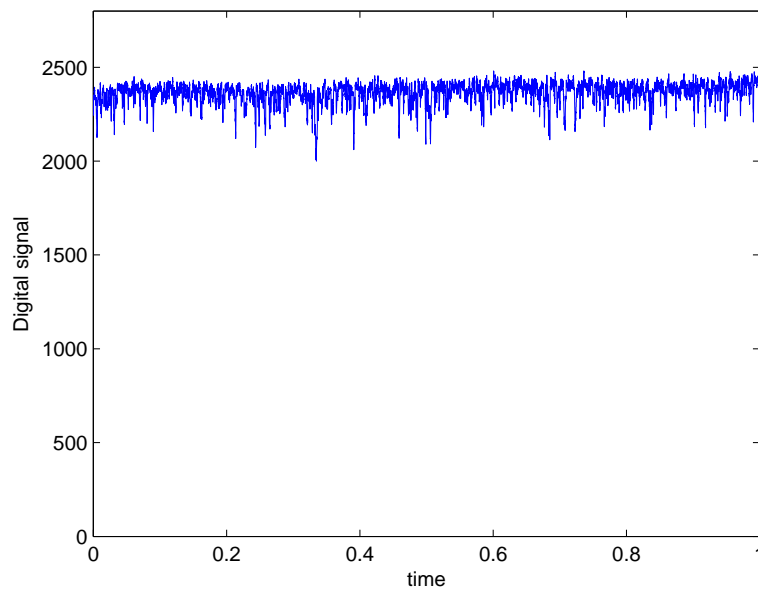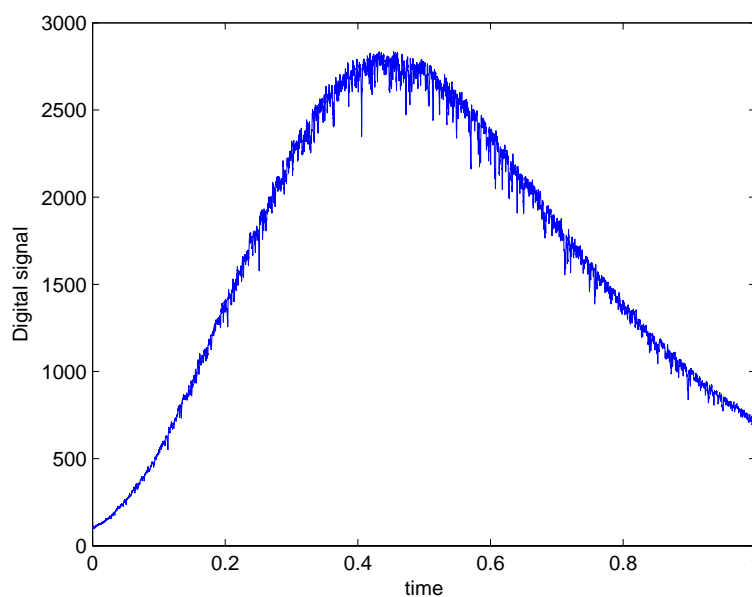

Figure 4.15: Measurement with 10kHz. Concentration as a function of time for one node of the outlet sensor at liquid flowrate 1500ml/min and gas flowrate 108sccm. Tracer pulse injected.

In order to filter out the influence that the bubbles have on the signal an enveloping curve could be fitted. This approach is motivated by the assumption that the peaks of the signal represent a situation without bubbles in the node. Like this the conductivity of the liquid phase could be reconstructed.

However, what is believed to be more promising is to make more measurements of the same kind in order to have a higher statistical relevance. In a second step the focus should be on the identification of effects that the gas phase has on the axial dispersion coefficient. This probably requires to investigate in much more detail the interconnection of holdup, bubble-size distribution, two-phase pressure drop and other parameters of the flow.

4.3   Additional Measurements

4.3.1   Pressure Drop

In an auxiliary measurement campaign the pressure drop over the packings
is measured. The result of these measurements is shown in Figure 4.16.
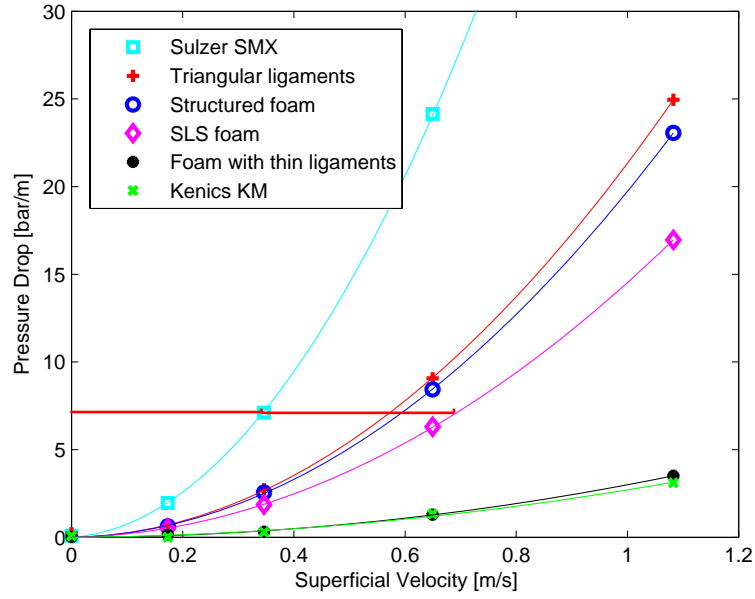
Figure 4.16: Pressure drop as a function of superficial velocity for five plastic
packings and one SLS packing. Fitted curves according to Forchheimer
model for pressure drop through porous media

Two approaches of pressure drop modeling are applied. The Forchheimer
equation for pressure drop of a flow through porous media is given by:

$$-\frac{dP}{dx} = \frac{\eta}{k_1} \cdot v + \frac{\rho}{k_2} \cdot v^2 \qquad (4.6)$$

where v is the superficial velocity, k_1 the darcian permeability coefficient
and k_2 the non-darcian permeability coefficient.

Another way to asses the pressure drop is by the friction factor. Differ-
ent definitions of the friction factor are known, like Fanning friction factor,
Darcy friction factor or Newton number [38]. In this thesis the Fanning
friction factor was used which is given by:

$$f = \frac{\Delta P \cdot d}{\rho v^2 2L} \qquad (4.7)$$

The estimated parameters of the Forchheimer equation and the estimated Fanning friction factor are shown in Table 4.3.

Table 4.3: Pressure drop modeling. Estimated parameters for Forchheimer equation and Fanning friction factor

	Forchheimer $k_1 \cdot 10^6$	Forchheimer k_2	Fanning friction factor: f
Sulzer SMX	0.464	18.62	208.11
Triangular ligaments	2.095	47.98	76.90
Structured foam	1.673	52.29	71.84
SLS foam	1.600	71.95	54.14
Structured foam with thin ligaments	23.020	338.66	11.91
Kenics KM	4.266	404.32	7.32

Comparing the different geometries it is observed that there are big differences among them. The Sulzer SMX has by far the highest pressure drop. One of the reasons is that it has a low porosity. A further explanation could be the sharp edges of this mixer, which was found by Bäriswyl [41] to have a major impact on the pressure drop. Also the packing with triangular ligaments has very sharp edges. That is a possible explanation why this packing has the second highest pressure drop.

The foams show a lower pressure drop than the packing with triangular ligaments. The plastic foam was measured to have a slightly higher pressure drop than the SLS foam. With a pressure drop of 17bar/m at the highest investigated velocity the SLS foam has the potential to be used in reactors of several meters length. The plastic foam with thin ligaments shows a pressure drop that is six times lower than the plastic foam with thick ligaments. For a discussion on these two structures see Chapter 3.4.2. What we conclude is that the high sensitivity of pressure drop on ligament shape and thickness raises hope regarding the potential of future improvements of the structure.

Last but not least we observe that the Kenics KM packing shows the lowest pressure drop. This makes Kenics KM an interesting candidate when dealing with non-catalyzed reactions. For catalyzed reactions the surface area of this structure is just too low.

4.3.2   Porosity

The porosity of the plastic structures was measured gravimetrically. For this
the mass, the length and both the inner and outer diameter of the packings
was measured. The density is known from the manufacturer data sheet to be
$\rho = 1130\text{kg/m}^3$. From the length and the outer and inner diameter we can
calculate the mass of the tube. Subtracting this mass from the total weight
we obtain the mass of the packing. Knowing the volume of the packing from
the inner diameter and the length we can calculate the porosity. Table 4.4
shows the porosity of the investigated packings.

Table 4.4: Measured porosity of plastic packings.

	Porosity [%]
Sulzer SMX	40.13
Triangular ligaments	71.59
Structured foam	75.68
Structured foam with thin ligaments	80.93
Kenics KM	78.87

It is observed that the Sulzer packing has a very low porosity. From the
CAD model a porosity of 50% was expected. We conclude that here the
manufacturing process deposited more material than intended. The highest
porosity was measured in the foam with thin ligaments. The Kenics mixer
lies in the similar region. In the structured foam packing, which is the one
that we are mainly interested, the porosity is over 75% what is a very good
value in terms of achieving a low pressure drop combined with a high specific
surface.

Chapter 5

Conclusions

Radial dispersion behavior of four static mixing devices is investigated by LIF and a WMS. As the results are not identical, LIF is chosen to be preferred because it has a higher resolution and is broadly accepted as the standard method.

Already at the lowest investigated flowrate the Sulzer SMX mixer shows a good mixing performance, quantified by a CoV of 0.02. For the other investigated packings a CoV of above 0.3 is observed at the same conditions. Due to intensified turbulence with increasing Reynolds numbers, the mixing performance steadily increases for all geometries except the Sulzer SMX. The small significance of the trend does not allow to draw a final conclusion wheter this is a physical effect or an artifact of the measurements.

Further it is observed that the industrially applied mixers show a slightly better mixing performance than our designs. This is explained by the smaller scale of the lamination in our geometries.

In an ancillary measurement campaign the pressure drop of the packings is determined. It is found that the Sulzer SMX packing has by far the highest pressure drop. The Fanning friction factor is estimated to be almost four times higher than in an SLS foam. The SLS foam is estimated to have a pressure drop of below 15bar/m at a superficial velocity of 1m/s. This makes SLS foams a potential structure for tubular reactors of several meters length.

Axial dispersion is measured with a wire-mesh sensor for the first time. To prove the concept, the RTD is measured in a single-phase flow. It is observed that a premixer affects the measurement of axial dispersion. In agreement with literature [2] we conclude that the axial dispersion coefficient is a function of the length of the investigated packing. This thesis proposes to explain this by the not fully developed flow at the entrance section of the packing.

Axial dispersion is therefore measured with a premixer that ensures that the entrance section is not included in the measurement. The estimated dispersion coefficients in single-phase flow through an SLS foam agree with the measurements done with standard electrodes in an earlier work of the LTR lab [43]. It is observed that the dispersion coefficient increases with increasing Reynolds number. An empiric formula fitted to the measurement data allows to estimate the RTD of a reactor of arbitrary length and flowrate. It is further shown that a narrow RTD is promoted by high flowrates even though the dispersion coefficient is higher in that case.

Axial dispersion in a multi-phase flow of air and water is investigated by means of a wire-mesh sensor. It is observed that the estimated dispersion coefficients show a high scattering. No conclusion about the effects of the gas phase on the axial dispersion in the liquid can be drawn.

Chapter 6

Outlook

6.1 Deeper Understanding of Entrance Length

From a scientific point of view it is of interest to more deeply investigate the entrance section of a flow through a foam.

One possibility to assess entrance behavior is by measuring velocity fields. The required tomographic investigations within a porous structure can be done by PIV. The challenge when measuring in solid structures is that an optical access is required. One way of solving this is to manufacture the structure from a transparent solid. To avoid refraction of the laser beam, the liquid has to be index matched to the solid.
From the evolution of turbulence at the packing inlet the length it needs to reach steady state can be determined.

Another possibility to assess the entrance behavior is to measure the axial dispersion coefficient in packings of different length. With increasing length the dispersion coefficient approaches a constant value. The interconnection of dispersion with turbulence allows then to identify the entrance length of the packing.

6.2 Axial Dispersion in Two-Phase Flow

The axial dispersion in the liquid phase of a gas-liquid two-phase flow was measured within this thesis. The results show a large scattering, making an interpretation of the data difficult. Performing more measurements to obtain a higher statistical relevance of the data one can obtain data which allows to identify clearer trends.

One difficulty in gas-liquid systems is that the density of the gas changes with pressure. As there is always a pressure drop in the tubular reactors, the fluiddynamics are always changing along the axis of the reactor. This makes it difficult to study the mechanisms which affect the axial dispersion. In a liquid-liquid two-phase flow it is possible to create constant conditions along a certain length of a reactor. In such a system mechanisms influencing the RTD in two-phase flow can be easier assessed.

6.3 Optimizing Packing Geometry

Further research activity should focus on how changes in the packing geometry influence the flow behavior. In the measurements of pressure drop it was observed that a small change in ligament thickness can have a very high impact on the pressure drop. Also radial mixing performance and RTD can be very sensitive to small changes in the packing geometry. A study should therefore optimize a packing for a certain application. Main parameters to investigate are ligament shape, ligament size, pore size and cell size.

Bibliography

[1] Han N.-W., Bhakta J., Carbonell R.G., 1985. Longitudinal and lateral dispersion in packed beds: effect of column length and particle size distribution. *AlChe Journal*, $31 - 2$, $277 - 288$.

[2] Delgado J.M.P.Q., 2006. A critical review of dispersion in packed beds. *Heat Mass Transfer*, 42, $279 - 310$.

[3] Paine M.A., Carbonell R.G., Whitaker S., 1983. Dispersion in pulsed systems - Heterogeneous reaction and reversible adsorption in capillary tubes. *Chemical Engineering Science*, $38 - 11$, $1781 - 1793$.

[4] Hobbs D.M., Muzzio F.J., 1998. Reynolds number effects on laminar mixing in the Kenics static mixer. *Chemical Enginering Journal* 70, $93 - 104$.

[5] Reinecke N., Boddem M., Petritsch G., Mewes D., 1996. Tomographisches Messen der relativen Phasenanteile in zweiphasigen Strömungen fluider Phasen. *Chemie Ingenieur Technik* 68, $1404 - 1412$.

[6] Boyer C., Duquenne A.-M., Wild G., 2002. Measuring techniques in gas-liquid and gas-liquid-solid reactors. *Chemical Engineering Science* 57, $3185 - 3215$.

[7] Hutter C., Allemann C., Kuhn S., Rudolf von Rohr Ph., 2010. Scalar transport in a milli-scale metal foam reactor. *Chemical Engineering Science* 65, $3169 - 3178$.

[8] Hutter C., Zenklusen A., Kuhn S., Rudolf von Rohr Ph. 2010. Large eddy simulations of flow through a streamwise-periodic structure. *Chemical Engineering Science*, **In review**.

[9] Hutter C., Zenklusen A., Lang R., Rudolf von Rohr Ph., 2010. Axial dispersion in metal foam and streamwise-periodic porous media. *Chemical Engineering Science*, **In review**.

[10] Ferrouillat S., Tochon P., Peerhossaini H., 2006. Micromixing enhancement by turbulence: Application to multifunctional heat exchangers. *Chemical Engineering and Processing* 45, $633 - 640$.

[11] Prasser H.-M., Böttger A., Zschau J., 1998. A new electrode-mesh tomograph for gas-liquid flows. *Flow Measurements and Instrumentation* 9, $111 - 119$.

[12] Prasser H.-M., Scholz D., Zippe C., 2001. Bubble size measurement using wire-mesh sensors. *Flow Measurement and Instrumentation* 12, $299 - 312$.

[13] Nalitham R.V., Davies O.L, 1987. Residence time distribution studies in a multiphase reactor under high temperature and pressure conditions. *Ind. Eng. Chem. Res.* 26, $1059 - 1066$.

[14] Trachsel F., Günther A., Khan S., Jensen K.F., 2005. Measurement of residence time distribution in microfluidic systems. *Chemical Engineering Science* 60, $5729 - 5737$.

[15] Banhart J., 2001. Manufacture, characterisation and application of cellular metals and metal foams. *Progress in Materials Science* 46, $559 - 632$.

[16] Fourie J.G., Du Plessis J.P., 2002. Pressure drop modelling in cellular metallic foams. *Chemical Engineering Science* 57, $2781 - 2789$.

[17] Du Plesis P., Montillet A., Comiti J., Legrand J., 1994. Pressure drop prediction for flow through high porosity metallic foams. *Chemical Engineering Science* 49, $3445 - 3553$.

[18] Stemmet C.P., Jongmans J.N., van der Schaaf J., Kuster B.F.M., Schouten J.C., 2005. Hydrodynamics of gas-liquid counter-current flow in solid foam packings. *Chemical Engineering Science* 60, $6422 - 6429$.

[19] Stemmet C.P., van der Schaaf J., Kuster B.F.M., Schouten J.C., 2006. Solid foam packings for multiphase reactors - Modelling of liquid holdup

and mass transfer. *Chemical Engineering Research and Design* 84, $1134 - 1141$.

[20] Stemmet C.P., Meeuwse M., van der Schaaf J., Kuster B.F.M., Schouten J.C., 2007. Gas-liquid mass transfer and axial dispersion in solid foam packings. *Chemical Engineering Science* 62, $5444 - 5450$.

[21] Richardson J.T., Peng Y., Remue D., 2000. Properties of ceramic foam catalyst supports: pressure drop. *Applied Catalysis A: General* 204, $19 - 32$.

[22] Richardson J.T., Remue D., Hung J.-K., 2003. Properties of ceramic foam catalyst supports: mass and heat transfer. *Applied Catalysis A: General* 250, $319 - 329$.

[23] Ergun S., Orning A.A., 1949. Fluid flow through randomly packed columns and fluidized beds. *Industrial and Engineering Chemistry* 41, $1179 - 1184$.

[24] Wadley R., Dawson M.K., 2005. LIF measurements of blending in static mixers in the turbulent and transitional flow regimes. *Chemical Engineering Science* 60, $2469 - 2478$.

[25] Mokrani A., Castelain C., Peerhossaini H., 2009. Experimental study of the influence of the rows of vortex generators on turbulence structure in a tube *Chemical Engineering and Processing* 48, $659 - 671$.

[26] Habisreuther P., Djordjevic N., Zarzalis N., 2009. Statistical distribution of residence time and tortuosity of flow through open-cell foams. *Chemical Engineering Science* 64, $4943 - 4954$.

[27] Hiby J.W., 1979. Definition und Messung der Mischgüte in flüssigen Gemischen. *Chem.-Ing.-Tech* 51, $704 - 709$.

[28] Zalc J.M., Szalai E.S., Muzzio F.J., 2002. Characterization of flow and mixing in an SMX static mixer. *AIChE Journal* 48, $427 - 436$.

[29] Zalc J.M., Szalai E.S., Muzzio F.J., 2003. Mixing dynamics in the SMX static mixer as a function of injection location and flow ratio. *Polymer Engineering and Science* $43 - 4$, $875 - 890$.

[30] Hirschberg S., Koubek R., Moser F., Schöck J., 2009. An improvement of the Sulzer SMX static mixer significantly reducing the pressure drop. *Chemical Engineering Research and Design* 87, 524 − 532.

[31] Levenspiel O., Smith W.K., 1957. Notes on the diffusion-type model for the longitudinal mixing of fluids in flow. *Chemical Engineering Science* 6, 227 − 235.

[32] Du Plessis J.P., 1994. Analytical quantification of coefficients in the Ergun equation for fluid friction in a packed bed. *Transport in porous media* 16, 189 − 207.

[33] Carberry J.J., Bretton R.H., 1958. Axial dispersion of mass in flow through fixed beds. *AIChE Journal* 4, 367 − 375.

[34] Levenspiel O., 1999. *Chemical Reaction Engineering*, John Wiley & Sons.

[35] Pope S.B., 2005. *Turbulent Flows*, Cambridge University Press.

[36] Kraume M., 2003. *Mischen und Rühren*, John Wiley & Sons.

[37] Hill C.G., 1977. *An Introduction to Chemical Engineering Kinetics & Reactor Design*, John Wiley & Sons.

[38] Paul E.L., Atiemo-Obeng V.A., Kresta S.M., 2004. *Handbook of Industrial Mixing - Science and Practice*, John Wiley & Sons.

[39] Evans L.C., 1998. *Partial Differential Equations*, American Mathematical Society.

[40] Hutter C., 2010. *Laser sintered meso scale reactor by design: characterization of heat and mass transfer*, Doctoral Thesis, ETH.

[41] Bäriswyl D., 2010. *Simulation of single-phase flow through porous media*, Bachelor Thesis, ETH.

[42] Viereck S., 2009. *Characterization of multiphase flow downstream structured porous media*, Bachelor Thesis, ETH.

[43] Zenklusen A., 2008. *Investigation of axial dispersion and simulation of flow within metal foam*, Master Thesis, ETH.

[44] Allemann C., 2008. *Characterization of mass transfer in metal foams*, Master Thesis, ETH.

Appendix A

LIF Images

This appendix shows examples of LIF images with the straight injection capillary experiments.
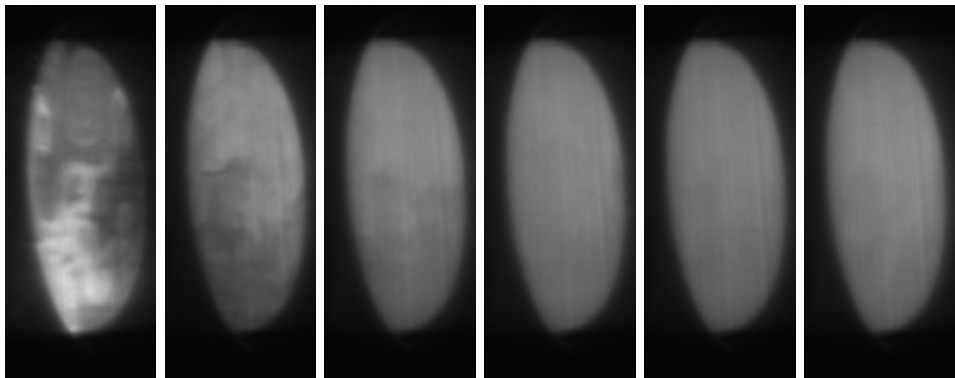

Figure A.1: Structured Foam. Sample LIF image for flowrates (from left to right) of 100, 200, 400, 800, 1500 and 2500ml / min.
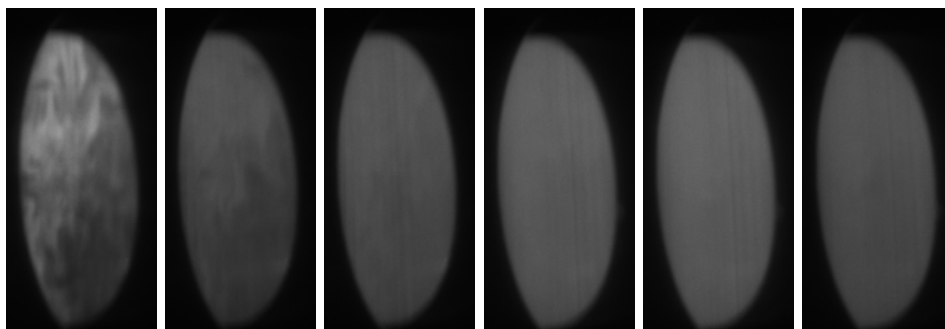
Figure A.2: Triangular Ligaments. Sample LIF image for flowrates (from left to right) of 100, 200, 400, 800, 1500 and 2500ml / min.
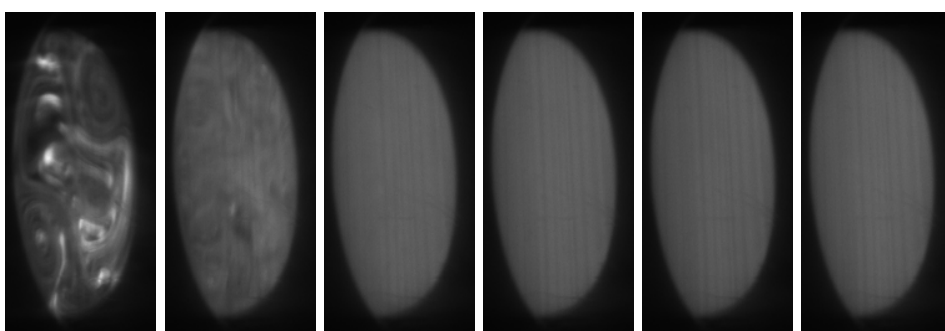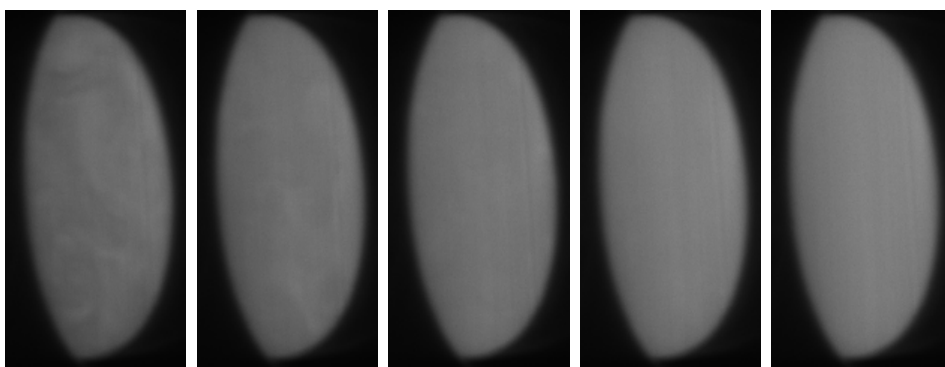

Figure A.3: Kenics KM. Sample LIF image for flowrates (from left to right) of 100, 200, 400, 800, 1500 and 2500ml / min.

Figure A.4: Sulzer SMX. Sample LIF image for flowrates (from left to right) of 100, 200, 400, 800, 1500ml / min.

Appendix B

WMS Images

This appendix shows the time averaged concentration distribution at the outlet of the packings as measured by the wire-mesh sensor. The range of the colorbar was chosen to be equal for all experiments in order to allow a comparison between them.
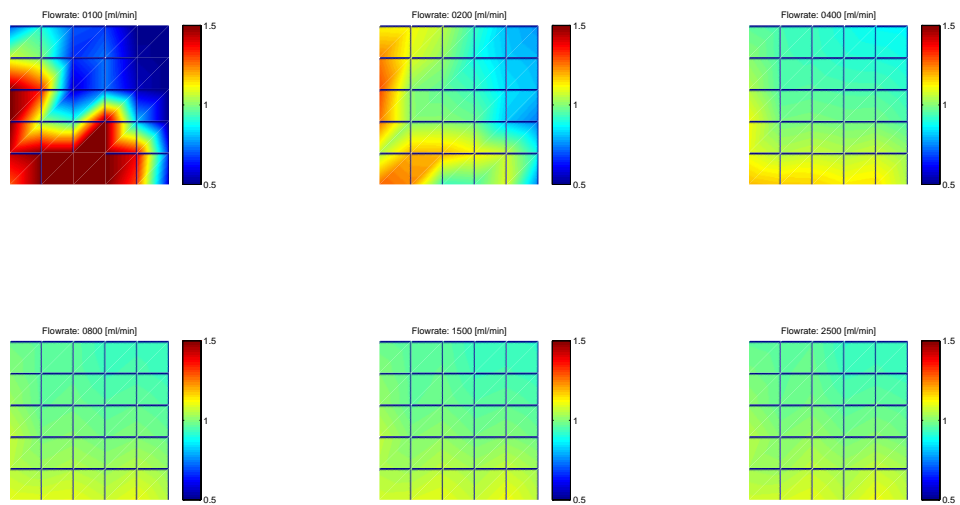

Figure B.1: Structured foam. Radial concentration distribution measured with wire-mesh sensor.
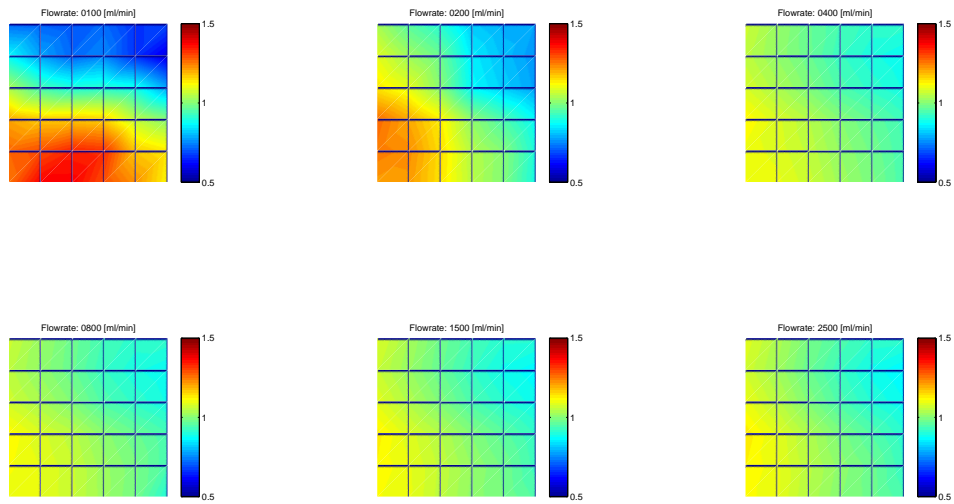
Figure B.2: Triangular ligaments. Radial concentration distribution measured with wire-mesh sensor.
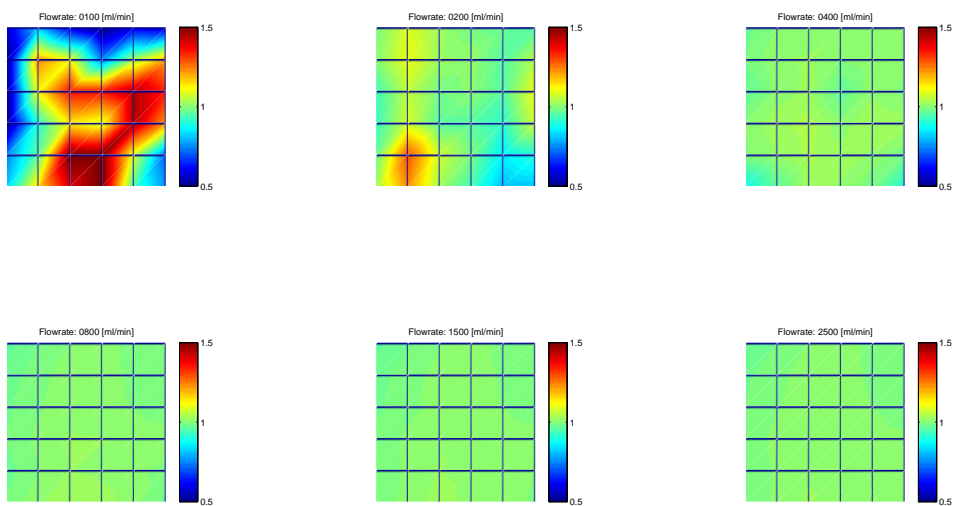

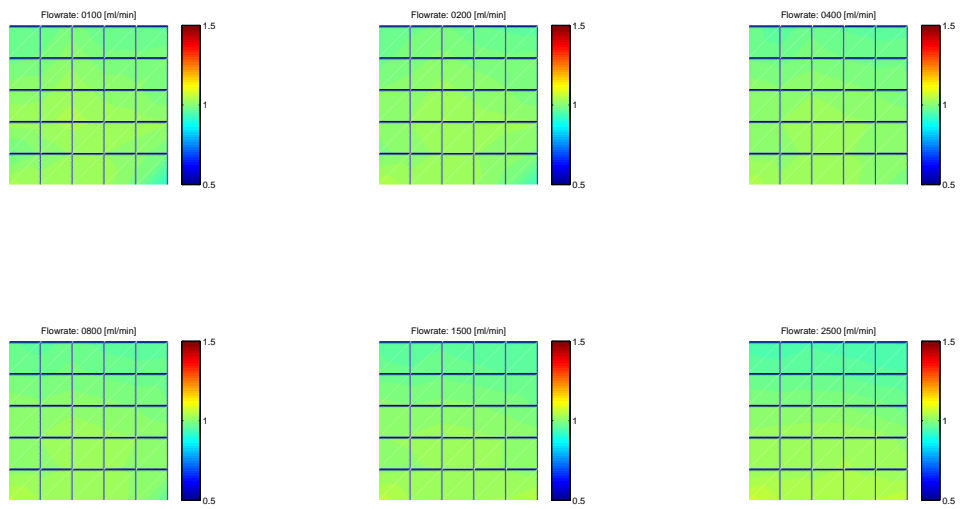Figure B.3: Kenics KM. Radial concentration distribution measured with wire-mesh sensor.

Figure B.4: Sulzer SMX. Radial concentration distribution measured with wire-mesh sensor.